



OPEN

Circadian rhythm and aryl hydrocarbon receptor crosstalk in bone marrow adipose tissue and implications in leukemia

Bihter Muratoğlu^{1,2}, Cansu Özdemir^{1,2}✉, Cemil Can Eylem³, Tuba Reçber³, Emirhan Nemutlu³, İdil Yet⁴ & Duygu Uçkan-Çetinkaya^{1,2,5}✉

Leukemic cells modulate the bone marrow microenvironment to enhance their survival. Lipolysis in bone marrow adipose tissue (BMAT) has emerged as a critical factor supporting leukemic cell survival, yet understanding its primary role in leukemia development remains limited. Fanconi anemia (FA), characterized by a predisposition to acute myeloid leukemia (AML) and hypersensitivity to environmental toxins, is a transitional model for studying leukemic transformation. Integrated multi-omics analyses were conducted on BMAT-derived mesenchymal stem/stromal cells (MSCs) from healthy donors (HD), AML, and FA patients. These analyses revealed intricate interactions among genes, metabolites, and lipids. Particularly noteworthy were the effects observed following the inhibition of aryl hydrocarbon receptor (AhR) signaling by StemRegenin1 (SR1). BMAT-MSCs showed increased expression of epithelial-mesenchymal transition (EMT) genes in FA and AML, suggesting a potential shift towards cancer-associated fibroblasts in the dysregulated marrow microenvironment. Identification of potential circadian rhythm biomarkers (*NPAS2*, *PER2*, *BHLHE40*, *PER3*, *CIART*) in BMAT-MSCs indicates a link between related lipid metabolism genes (e.g., *PTGS1*, *PIK3R1*) and SR1 treatment, implicating them in lipolysis processes. Dysregulation of circadian rhythm-related genes (*CIART*, *BHLHE40*, *NPAS2*) in AML BMAT-MSCs, along with changes in circulating lipid metabolites like palmitate suggests their role in shaping the leukemia microenvironment. Upregulation of *FABP5* and *CD36* suggests a novel molecular mechanism involving *FABP5* in AhR-mediated circadian regulation and identifies *CD36* as a potential partner for *FABP5* in BMAT-MSCs. Overall, this study unveils the interplay between AhR signaling, circadian rhythm, and the leukemia microenvironment in BMAT-MSCs, offering new insights into leukemia pathogenesis and therapeutic opportunities.

Keywords Bone marrow adipose tissue, Circadian rhythm, AhR signaling, Multi-omics, AML, Fanconi anemia

Bone marrow (BM) is the primary site for hematopoiesis, where both cellular and non-cellular components create a niche for hematopoietic stem cells (HSCs) and their progeny to perform their life-long functions. Mesenchymal stem/stromal cells (MSCs) are key elements of the BM microenvironment, supporting this niche by differentiating into adipocytes, osteoblasts, and by secreting soluble factors and extracellular matrix components¹. Among the cellular components, adipocytes have garnered significant attention in the pathogenesis of leukemia. They are active participants in the metabolic crosstalk with HSCs and leukemic cells².

BM adipocytes possess unique properties, distinguishing them from both white and brown adipocytes³. The bone marrow adipose tissue (BMAT) is characterized by a cholesterol-based metabolism rather than being primarily lipolytic⁴. Research has indicated that, in the early stages of leukemia, BM adipocytes contribute to establishment of a microenvironment that supports tumor growth⁵. However, the extensive proliferation of leukemic blasts in the BM leads to a rapid reduction in these adipocytes. The literature on how leukemic cells

¹Center for Stem Cell Research and Development (PEDI-STEM), Hacettepe University, 06100 Sıhhiye, Ankara, Turkey. ²Department of Stem Cell Sciences, Institute of Health Sciences, Hacettepe University, 06100 Sıhhiye, Ankara, Turkey. ³Department of Analytical Chemistry, Faculty of Pharmacy, Hacettepe University, 06100 Sıhhiye, Ankara, Turkey. ⁴Department of Bioinformatics, Institute of Health Sciences, Hacettepe University, 06100 Sıhhiye, Ankara, Turkey. ⁵Division of Hematology, Department of Pediatrics, Hacettepe University Faculty of Medicine, 06100 Sıhhiye, Ankara, Turkey. ✉email: cansuozdemir@hacettepe.edu.tr; duygu2008@gmail.com

regulate adipocytes and their impact on disease progression is limited. Recent investigations have revealed that a diminished size of BM adipocytes is associated with a poor prognosis in acute myeloid leukemia (AML), with AML patients exhibiting significantly smaller adipocytes compared to the control group⁶. Another study has provided evidence that AML blasts remodel the BM niche by releasing exosomes, thereby creating a microenvironment that favors leukemia growth while simultaneously suppressing normal hematopoiesis⁷. However, little is known about how leukemia cells alter the BM niche to facilitate their growth and evade chemotherapy.

Dioxins/xenobiotics and dioxin-like compounds are toxic substances that emerge as industrial byproducts and are highly harmful to biological systems⁸. Aryl Hydrocarbon Receptor (AhR), also known as the dioxin receptor, serves as the main regulator of dioxin-mediated toxic substances⁹. AhR and circadian clock pathways are integrated and exhibit reciprocal regulation, as established in the literature¹⁰. The circadian clock is an evolutionarily conserved system. It consists of endogenous oscillators that regulate the organism's physiological processes and various metabolic functions. These rhythmic oscillations are necessary for functions such as adaptation to environmental stimuli like day-night cycles, sleep-wake cycles, nutrition, and hormone release. The circadian clock operates through the transcription-translation feedback loop (TTFL) at the molecular level. Four key circadian clock genes, BMAL1 (Brain and Muscle ARNT-Like 1 or Aryl hydrocarbon receptor nuclear translocator-like protein 1 (ARNTL)) and CLOCK (Circadian Locomotor Output Cycles Kaput), are responsible for positive regulation. At the same time, CRY (CRYPTOCHROME) and PER (PERIOD) are responsible for negative regulation¹¹.

AhR and ARNT have exhibited significant homology with the core circadian clock genes, CLOCK and BMAL1. These proteins belong to the bHLH/PAS domain-containing family. They are particularly known for their roles as regulators of circadian rhythms, mediators of responses to hypoxia, and contributors to xenobiotic metabolism^{12,13}. Research has shown that increased levels or activity of circadian clock components (e.g., CLOCK: BMAL1) can inhibit tumor growth and proliferation. In this context, various chronotherapeutic interventions aim to improve or restore circadian rhythms to suppress cancer development and enhance response to anticancer treatments. On the other hand, some studies have shown that core clock genes, such as those found in leukemia stem cells, may exhibit tumor-promoting functions depending on the cancer cell state or type¹⁴ resulting in differentiation and expansion of leukemia stem cells that propagate the disease¹⁵.

The circadian clock regulates a diverse number of metabolic pathways, affecting key metabolic enzymes transcriptionally through the CLOCK-BMAL1 heterodimer, as well as influencing metabolically active tissues indirectly by regulating endocrine factor release in a time-of-day-dependent manner¹⁶. Given the critical roles of AhR and the circadian clock in glucose and lipid metabolism regulation, desynchronized AhR activity is expected to impact metabolic functions¹⁷. Moreover, AhR deficiency leads to changes in circadian-controlled metabolites such as glucose, insulin, and triglycerides, underscoring the involvement of AhR in circadian regulation¹⁸.

Understanding the cellular and molecular mechanisms driving BMAT expansion and its interaction with cancerous cells is crucial for developing novel therapies to enhance BM health. Moreover, BMAT biology is a new research area with many unknowns, supporting the elucidation of numerous mechanisms awaiting clarification related to BM biology and the leukemogenesis process. This exploration can deepen our comprehension of how BMAT influences its metabolism and that of tumor cells. On the other hand, the impact of BMAT on normal hematopoiesis is contentious in the literature.

Studies have suggested that the circadian clock regulates approximately 10–40% of the transcriptome^{19,20}, and around 50% of metabolites exhibit oscillating levels in response to circadian rhythms²¹. Based on the information indicating its widespread regulatory effect, we aimed to delineate the potential effects of BMAT-MSCs on AML pathogenesis through the crosstalk between the circadian clock and AhR signaling after treatment with AhR antagonist StemRegenin1 (SR1). The literature recognizes a relationship between the circadian clock and leukemogenesis. However, unraveling this complex interplay requires a holistic analysis of pathways. In addition to the intrinsic events in HSCs, how stromal cells and adipocytes effect HSC biology and leukemogenesis through circadian clock regulation perspective is the most unknown side of the mechanisms.

From this point, we conducted a comprehensive study employing a multi-omics approach that included RNA sequencing-based transcriptomics, as well as gas chromatography-mass spectrometry (GC-MS) and liquid chromatography-quadrupole time-of-flight mass spectrometry (LC-QTOF-MS) for metabolomics and lipidomics analysis. This multi-omics analysis provided a holistic understanding of biological processes because it considers the interplay between genes, metabolites, and lipids. The study focused on BMAT-MSCs from healthy human donors (HD), patients with AML, and patients with Fanconi anemia (FA)—a hereditary disease characterized by DNA double-strand breaks, hypersensitivity to xenobiotics, and a predisposition to the development of myeloproliferative diseases/AML^{22–24}.

Methods

Cell culture

Bone marrow samples were collected from 3 HD, 3 patients with FA, and 3 patients with AML. Patients with FA did not show signs of leukemia or myelodysplastic syndrome at the time of collection. Sample nomenclature and information list are shown in Supplementary Table 1. BMAT-MSCs were isolated following the International Bone Marrow Adiposity Society (BMAS) guidelines^{25,26}. Bone marrow aspiration samples were centrifuged at 453g for 10 min to obtain a BMAT fraction. The fatty layer was collected, plasma was separated, and mononuclear cells were obtained by Lymphoprep centrifugation at 1050g for 25–30 min at room temperature without brake. Cells were cultured in low-glucose Dulbecco's Modified Eagle Medium (LG-DMEM) (Biowest) supplemented with penicillin-streptomycin (100 U/ml and 100 µg/ml, respectively), 1% L-Glutamine (Biowest), and 10% FBS (Gibco) in a humidified incubator at 5% CO₂ and 37 °C. Adherent cells at 80–90% confluency were passaged, and experiments were conducted at passage 3. Immunophenotyping was performed using (Supplementary Fig. 1) CD105-APC (BioLegend, #32320), CD29 (BioLegend, #303003), and negative markers CD45-FITC

(BioLegend, #304006) and CD34 (BioLegend, #343503) on the BD Accuri C6 v1.0 system. Osteogenic and adipogenic differentiation potential was assessed using StemPro kits (StemPro, #A1007201, and #A1007001, respectively). Osteogenic differentiation was assessed based on calcium deposition and visualized using phase-contrast imaging. Adipogenic differentiation was evaluated using Oil Red O staining to visualize lipid droplet formation. As a control, undifferentiated BMAT-MSCs were maintained under standard culture conditions for 14 days. All images were captured using an inverted light microscope. Results are shown in Supplementary Fig. 2.

Circadian synchronization

BMAT-MSCs were seeded into 6-well plates at 1×10^6 cells per well. After seeding, the medium was supplemented with 100 nM Dexamethasone (DEX) (Sigma-Aldrich, #50-02-2), and the plates were incubated for 1 h. Cells were then collected at the 18th hour and stored at -80°C in 500 μL of QIAzol until RNA extraction (Qiagen, #79306).

Cell proliferation assay

Cell proliferation was evaluated via WST-1 assay (Roche, #11644807001). Cells were plated in 96-well plates and treated with different StemRegenin1 (SR1) (STEMCELL Technologies, #72342) concentrations, an AhR antagonist. After incubation, WST-1 reagent was added, and absorbance at 450 nm was measured using a microplate reader (TECAN ELISA reader). Absorbance values were normalized to untreated control cells.

AhR antagonist treatment

To investigate the entrainment of the circadian clock in BMAT-MSCs using the AhR antagonist SR1 in vitro, we utilized DEX and SR1 dissolved in ethanol and DMSO, respectively. Cells were plated in 6-well plates at a concentration of 1×10^6 cells and incubated overnight. The next day, after synchronization, cells were treated with SR1 at a final concentration of 1.5 μM based on the results of the WST-1 assay. Cell supernatants and BMAT cells were collected at ZT18 for metabolomics and transcriptomics analysis, respectively.

Transcriptomics analysis

The cell culture wells were washed with PBS, and cells were collected in 500 μL QIAzol Lysis Reagent (Qiagen #79306) for RNA isolation, which was performed with 100 μL chloroform (Merck #102445) and ethanol (Merck) precipitation. The RNA phase was separated by ultracentrifugation at 12,000g for 20 min. RNA precipitation was then carried out with a 1:1 v/v RNeasy Lysis Reagent/Isopropanol (Merck) mixture. The RNA pellets were washed with 1 ml of 75% ice-cold ethanol (Merck). The phenol-extracted RNA was further purified using the RNeasy Miniprep Kit (Qiagen #74104), with optional on-column DNase treatment, following the manufacturer's instructions. Samples collected at one time point (ZT18) were sequenced. A total of 18 samples were used for RNAseq experiments. Quality and quantity measurements of isolated total RNAs were analyzed using both the Nanodrop 1000TM spectrophotometer (Thermo Scientific, USA), Qubit (Thermo Fisher Scientific, USA), and BioAnalyzer (Agilent, USA). RNA samples with OD260/280 ratios between 1.8 and 2.0, 28 S:18 S ≥ 1 , and RNA integrity number (RIN) ≥ 8 were used for library construction. For each sample, cDNA libraries were generated from 1 μg total RNA using the Illumina Stranded Total RNA Library Prep with Ribo-Zero Plus Kit (Illumina #20040529), following the manufacturer's instructions. Paired-end 100-bp read cDNA libraries were prepared in three biological replicates per group, using the HiSeq2500 sequencing platform (Illumina, USA) through a commercial sequencing service.

cDNA synthesis from isolated total RNA was conducted using the Nepenthes kit (#NP041011610) for both RNAseq and transcriptomic data validation. qRT-PCR studies utilized GoTaq qPCR master mix (Promega #A6001) on a Roche Light Cycler 480 fluorometric PCR instrument. The housekeeping gene *ACTB* served as an internal control for mRNA abundance. Reactions were conducted with three biological replicates and three technical replicates per sample, including no-template controls (NTCs). Fold changes in target gene mRNA levels were calculated using the formula $2^{-(\Delta\Delta\text{Ct})}$. Gene list and primer sequences are available in Supplementary Table 2.

Metabolomics and lipidomics analysis

The metabolomic analysis involved utilizing two orthogonal metabolomics platforms: gas chromatography-mass spectrometry (GC-MS) and liquid chromatography quadrupole time-of-flight mass spectrometry (LC-qTOF-MS). Initially, 750 μL of cell culture supernatants were evaporated until dry using a vacuum centrifuge concentrator at room temperature (Labconco, refrigerated centriVap concentrator). Upon complete evaporation, a 900 μL mixture of methanol: water (9:1 v/v) was added to the pellet of metabolomics samples and centrifuged at $+4^\circ\text{C}$, 14,000 rpm for 10 min. 400 μL of supernatants were collected into new tubes and repeated evaporation under the same conditions. Subsequently, freshly prepared 20 μL of 20 mg/mL methoxyamine hydrochloride in pyridine (MeOX-Sigma-Aldrich) was added to the evaporated samples and vortexed, then, were incubated in a shaking oven at 37°C for 30 min. Following the incubation, 50 μL of *N*-Methyl-*N*-(Trimethylsilyl) trifluoroacetamide + 1% trimethylchlorosilane (Sigma, 69478) was added per sample and vortexed and then incubated in a shaking incubator at 30°C for 30 min for derivatization. Samples, after derivatization, underwent GC-MS analysis using a Shimadzu GCMS-QP2010 Ultra (Kyoto, Japan), utilizing a DB-5MS stationary phase column (30 m + 10 m Duraguard \times 0.25 mm i.d., with a film thickness of 0.25 μm). The temperature in the oven started at 60°C , maintained for 1 min, before ramping up from 60 to 325°C at a rate of 10°C per minute, where it remained for an additional 10 min. An injection volume of 1 μL was employed in a splitless mode. The mass-to-charge ratio (m/z) range for scanning the samples was set between 50 and 650.

For lipidomics analysis, the dried-out samples were resolved with 200 μ L chloroform by vortexing for 1 min. Subsequently, the tubes were centrifuged at 12,000 rpm for 10 min at +4 °C. The supernatant was transferred to new tubes and evaporated to dryness. The dried samples were reconstituted with 150 μ L of acetonitrile: isopropanol (7:3, v/v) mixture. The entire supernatant was transferred to the vials and then analyzed by LC-qTOF-MS (Agilent 6530 accurate-mass, California, USA). The analyses were performed in negative and positive ionization modes using a C18 (100 \times 2.1 mm, 2.7 μ m) column with mobile phases consisting of (A) water: acetonitrile (6:4, v/v) containing 10 mM ammonium formate (Fluka, #BCBQ4969V) and 0.05% formic acid (Merck, #64-18-6,) and (B) isopropanol: acetonitrile (9:1, v/v) containing 10 mM ammonium formate and 0.05% formic acid in gradient elution mode. The run time was 27 min and instrument parameters, and gradient elution were as previous study²⁷.

Identification of differentially expressed genes, metabolites, and lipids

Firstly, checks for barcode contamination, sequence adapters, and unmapped paired-end sequences were done, and a set of standard quality value calculations were performed using the FastQC (v0.11.9) (Babraham Bioinformatics, UK). To clean and enhance the quality of the reads, adapter sequences, sequences with a Phred score below 20 ($Q < 20$), bases containing unidentified bases (N) ($N > 5$), sequences shorter than 32 bases, and low bases in the 3' terminus of the sequences were trimmed using Trimmomatic software v0.39²⁸. Fastq files containing trimmed RNA-seq reads were aligned to the human reference genome GRCh38 by using STAR (v2.7.10b) (default parameters). STAR is especially used for RNAseq mapping²⁹. Mapping statistics can be found in Supplementary Table 3. After the mapping process, the Cuffdiff command in the Cufflinks suite was employed with default parameters. This utilized a false discovery rate (FDR) threshold of ≤ 0.01 to detect differentially expressed genes (DEGs) between different conditions³⁰. Differential expression analysis was conducted utilizing quartile library normalization, followed by calculation of fragments per kilobase of exon per million mapped reads (FPKM) and fold changes.

MS-DIAL (ver. 4.92) software was used to perform deconvolution, peak alignment, and retention time correction on complex chromatograms obtained by GC-MS and LC-qTOF-MS-based metabolomics and lipidomics analyses. Metabolites were identified by the Fiehn Retention Index Library. Lipids were identified with MS/MS spectral libraries (positive and negative, RIKEN) provided by the software manufacturer by comparing MS/MS spectra obtained by applying different energy levels (10, 20, and 40 eV). Data matrices from both GC-MS and LC-qTOF-MS analyses were separately normalized by QC samples-based LOESS algorithm (Locally Weighted Scatterplot Smoothing). After normalization, the data has been scaled according to the mean. The normalized data matrices were exported to .csv format and further curation of the data was carried out with Excel. Missing values in the data set were filled with half the value of the smallest relative concentration within the sample group. Metabolites and lipids containing higher than 50% missing values and identified in the mobile phase were excluded from the data matrix. The data integrity was evaluated using principal component analysis (PCA) (data not shown).

MetaboAnalyst v6.0 tool (<https://www.metaboanalyst.ca/>) was used for statistical and visualization of the metabolomics data. Whether the metabolites of the difference among AML, FA, and HD groups, differential expression metabolites (DEMs) were determined by the fold change and Student's t-test values ($p < 0.05$) and visualized by volcano plots (data not shown) and orthogonal partial least-squares discriminant analysis (OPLS-DA) (Supplementary Fig. 3A). LipidSuite (<https://suite.lipidr.org/>) was employed for statistical analysis and visualization of the lipidomics data. OPLS-DA (Supplementary Fig. 3B) and Student's t-test were utilized to identify differentiated groups. Univariate analysis, similar to DEMs, was used for differentially expressed lipids (DELs).

Functional enrichment analysis

The biological significance of DEGs was assessed through Gene Ontology (GO) analysis, covering biological process (BP), cellular component (CC), and molecular function (MF), utilizing the ShinyGO v8.0 (<http://bioinformatics.sdstate.edu/go/>) webtool. To further investigate enriched gene sets, we employed gene set enrichment analysis (GSEA) utilizing hallmark gene sets from MSigDB in ShinyGO v0.8 with default parameters.

Metabolite set enrichment analysis (MSEA) was performed using MetaboAnalyst v6.0 with default parameters. The statistically differentiated metabolites were matched with related pathways by scanning the KEGG database www.kegg.jp/kegg/kegg1.html^{31,32}.

Lipid Pathway Enrichment Analysis (LIPEA) software (<https://lipea.biotec.tu-dresden.de>) was employed to conduct pathway enrichment analysis of lipids using the Over Representation Analysis (ORA) approach.

Multi-omics integration of transcriptomics and metabolomics

The interaction pathways between DELs and DEGs were established using MetaboAnalyst v6.0's Joint-pathway analysis module. The results were then visualized with STITCH, a protein/compound query plugin in Cytoscape v3.10.1 (<https://cytoscape.org/>) to illustrate biological relationships between metabolites and genes.

Lipid pathway analysis was performed using BioPAN software (<https://www.lipidmaps.org/biopan>). Pathways with a p-value < 0.05 were considered significant. The most stimulated and inhibited lipid reactions were identified based on a Z-score > 1.645 .

Statistical analysis

GraphPad Prism v9.0.1 (GraphPad Software, USA) was utilized for data visualization and statistical analysis, including qRT-PCR analysis and classification of omics data. Gene expression analysis underwent statistical analysis using two-way ANOVA, followed by Fisher's LSD test for multiple comparisons. A significance level of $p < 0.05$ was applied to all experiments, and data are presented as mean \pm SEM. Additional details on statistical

tests conducted for each experiment, including qRT-PCR and multi-omics data, can be found in the figure legends. Criteria for screening DEMs and DELs included $p < 0.05$, Log2 Fold Change, and VIP > 1 , respectively.

Results

We conducted a study involving human BMAT-MSCs obtained from three HD, three patients with AML, and three patients with FA, an inherited disease characterized by AML predisposition. We investigated the biological role of crosstalk between the circadian clock and AHR signaling after treatment with 1.5 μM SR1 and compared the corresponding signaling pathway response with stromal cells obtained from bone marrow pathologies. We collected cells and cell culture supernatants under synchronized conditions (exposure to DEX for one hour at a concentration of 100 nM) at Zeitgeber Time 18. The workflow of our study, detailing the experimental design and multi-omics approaches in BMAT-MSCs exposed to SR1, is illustrated in Fig. 1.

Despite the natural variability in individual patient characteristics (Supplementary Table 1) such as age, gender, and disease subtype, the results from individuals within the same group were pooled and analyzed collectively. By normalizing treated samples to their respective untreated controls, the influence of individual variation was minimized, enabling the focus to remain on the specific effects of SR1 within each group (HD, FA, AML). This approach ensured that the observed differences could be attributed to SR1's impact on the groups rather than individual variability. However, the high interindividual variability inherent in human specimens, including those from healthy donors and patients, underscores the need for larger sample sizes in future studies to better define differences in baseline profiles.

Inhibition of AHR in BMAT-MSCs with SR1 treatment

We initially found that SR1 inhibits AhR signaling by reducing the expression of specific AhR target genes like *CYP1A1*, *CYP1B1*, and *TIPARP*, as shown in RNA-seq (Supplementary Table 4). Validation using qRT-PCR confirmed decreased *CYP1A1* expression levels following SR1 treatment compared to untreated CTRL groups, consistent with RNA-seq data (Fig. 2A). Furthermore, three genes (*PTGS1*, *NPAS2*, *PER2*) selected from RNA-seq results were validated with qRT-PCR, aligning with RNA-seq trends (Fig. 2B).

Evaluation of transcriptomics, metabolomics, and lipidomics data

Transcriptomics data involved exposing cells to SR1 treatment or untreated controls (CTRL), followed by total RNA isolation and sequencing as described in the “Methods” section. Transcriptome analysis was conducted on 18 samples (HD = 3, FA = 3, and AML = 3; SR1 and CTRL, respectively) in BMAT-MSCs, alongside metabolomics and lipidomics analyses. All data underwent quality control and trimming, with Phred scores (Q scores) ≥ 30 . Alignment to the human reference genome (GRCh38) revealed total mapping rates averaging 99.61% and 99.64% for each sample in CTRL and SR1, respectively (Supplementary Table 3), indicating high-quality data suitable for transcriptome analysis. Differentially expressed genes (DEGs) totaled 691 and 420 in SR1 and CTRL groups, respectively, with 194 genes overlapping.

In metabolomics data, the quality, reliability, and biological significance of results were assessed. Quality control samples were used to ensure data reliability and accuracy. Data were normalized to minimize technical variations and enable comparability across different experimental conditions. Metabolites and lipids with over 50% missing values, exhibiting a RSD value exceeding 30% in QC samples, and identified in the mobile phase content were excluded from the data matrix. A total of 159 metabolites and 88 lipids were identified with a score value greater than 70 by RI Fiehn library for metabolomics and matching of MS/MS spectra for lipidomic analyses.

Classification of all genes, metabolites, and lipids

The multi-omics analysis provided descriptive information for BMAT-MSCs. Untreated CTRL (Fig. 2C) and SR1 treatment (Fig. 2D) groups were differentiated to assess gene, metabolite, and lipid profiles. Genes were classified based on RNA types, while metabolites and lipids were categorized by chemical class. In transcriptomics data, most transcripts increased with SR1 treatment across various RNA types, with some specific RNA types observed only in the SR1 group. Notably, snoRNA (48) showed a significant upregulation post-treatment. Metabolomics data revealed 159 metabolites grouped into 12 classes, including carbohydrates, fatty acyls and nucleic acids. Lipidomics identified 88 lipid species across 7 classes, such as encompassing monoglycerides, diglycerides, sphingomyelins, and phosphatidylcholines.

Identification and visualization of differentially expressed genes (DEGs), metabolites (DEMs), and lipids (DELs)

Classical criteria ($p < 0.05$, Log2 Fold Change, and VIP > 1) were used to identify DEGs, DEMs, and DELs (Supplementary Tables 4, 5, 6, 7, 8). In the untreated CTRL group of BMAT-MSCs, significant DEGs were identified as 242, 77, and 242, DEMs as 6, 22, and 7, and DELs as 54, 18, and 44 for AML vs. HD, FA vs. HD, and AML vs. FA comparisons, respectively (Fig. 2E). Conversely, in the SR1 treatment group, significant DEGs were identified as 389, 148, and 429, DEMs as 25, 20, and 25, and DELs as 3, 49, and 11 for the same comparisons (Fig. 2F). Unique DEGs and DEMs markedly increased with SR1 treatment compared to the untreated CTRL group across all comparisons, except for DELs in the FA vs. HD comparison, which decreased sharply in AML vs. HD and AML vs. FA groups. Hierarchical clustering confirmed differences between hematological malignancies (AML and FA) and healthy donors for both SR1 treatment and untreated CTRL. Heatmaps (Fig. 2G–I for CTRL, and Fig. 2J–L for SR1 treatment) showed 50 differential genes ($\text{padj} < 0.05$) for transcriptomic data, and 80 metabolites and lipids for metabolomic and lipidomic data.

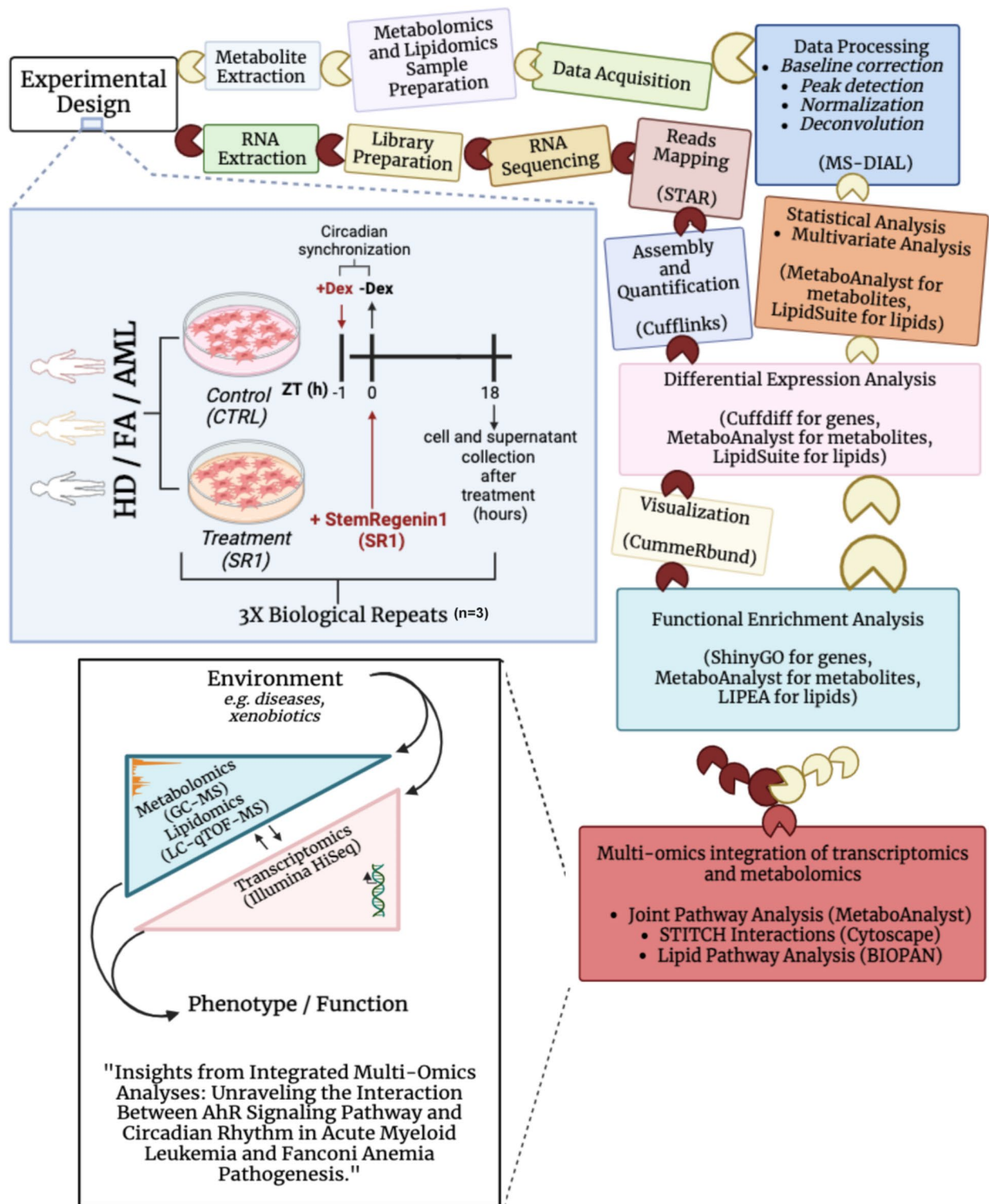


Fig. 1. The workflow of the study. Human bone marrow adipose tissue-derived mesenchymal stem cells (BMAT-MSCs) obtained from three healthy donors (HD), three patients with Acute Myeloid Leukemia (AML), and three patients with Fanconi Anemia (FA), an inherited disease characterized by AML predisposition, is depicted. Cells and cell culture supernatants were collected under synchronized conditions (dexamethasone (DEX) for one hour at of 100 nM) at Zeitgeber Time 18. The experimental design and multi-omics approaches employed in BMAT-MSCs exposed to SR1 are detailed. Created with BioRender.com.

Functional enrichment analysis of differentially expressed genes (DEGs), metabolites (DEMs), and lipids (DELs)

Gene ontology (GO) analysis of DEGs

GO analysis was conducted to discern key biological features from transcriptomic data, with results detailed in the top 20 GO terms across BP, CC, and MF (Fig. 3A–F). Notable GO-BP terms indicated significant regulation of cellular processes such as migration, morphogenesis, and locomotion with SR1 treatment in AML vs. HD and AML vs. FA comparisons (Fig. 3B,F). Additionally, untreated CTRL groups showed similar trends in AML vs. HD and AML vs. FA comparisons, with an overlap of 60% (Fig. 3A,E). While gene expression levels decreased overall compared to CTRL groups, top three enriched GO-CC terms remained consistent across all comparative groups, highlighting increased DEG numbers upon SR1 treatment (Fig. 3; middle). Moreover, distinct expression patterns were observed in SR1-treated groups compared to untreated CTRL, particularly in EMT-related processes (Fig. 3B; middle). This difference was underscored by alterations in the extracellular matrix and related genes, with notable changes in SR1-treated groups (Supplementary Table 9). Additionally, GO-MF analysis revealed significant increases in insulin binding function in AML vs. HD comparisons with SR1 treatment, indicating potential pathway alterations (Fig. 3B, right). These enriched terms offer insights into the role of DEGs in AhR inhibition.

Gene sets enrichment analysis (GSEA) of DEGs

Gene set enrichment analysis (GSEA) was conducted using ShinyGO v0.8, utilizing the R/Bioconductor package. Enriched gene sets from the MSigDB hallmark data collection were obtained, with a false discovery rate (FDR) threshold of 0.05. These gene sets are highly reliable and curated to include consistently observed genes in specific pathways. Hallmark genes were investigated across three comparative groups, including SR1 treatment and untreated CTRL, revealing overlapped hallmarks (highlighted in red in Fig. 4A,B). Seven significantly enriched hallmarks were observed with SR1 treatment, including epithelial-mesenchymal transition, hypoxia, TNF α signaling via NF κ B, IL6 jak stat3 signaling, cholesterol homeostasis, estrogen response early, and apoptosis (Fig. 4B). Notably, two of these hallmarks, epithelial-mesenchymal transition, and estrogen response early, also overlapped with untreated CTRL groups (Fig. 4A). Enriched genes showed at least a 2-fold increase after SR1 treatment compared to untreated CTRL. Additionally, hallmark adipogenesis and estrogen response late, absent in untreated CTRL groups, were considered, although not exhibiting the highest fold changes as the seven hallmarks.

Metabolite sets enrichment analysis (MSEA) of DEMs

Metabolite set enrichment analysis (MSEA) was conducted using MetaboAnalyst v6.0. Overlapped pathways were highlighted in a rectangle (Fig. 4C,D), revealing significantly enriched metabolites and pathways after SR1 treatment across all comparative groups. Eleven pathways overlapped among the three comparative groups after SR1 treatment, compared to only one pathway (arginine biosynthesis) in the untreated CTRL groups. Non-overlapped pathways (19) after SR1 treatment in the three comparative groups were examined in pairwise comparisons. Notable findings include the presence of the pyrimidine metabolism pathway in both AML vs. HD and FA vs. HD comparisons, and common pathways such as arginine biosynthesis, alanine, aspartate, and glutamate metabolism, and biosynthesis of unsaturated fatty acids in AML vs. HD and AML vs. FA comparisons. Similarly, the starch and sucrose metabolism pathways overlapped in FA vs. HD and AML vs. FA groups.

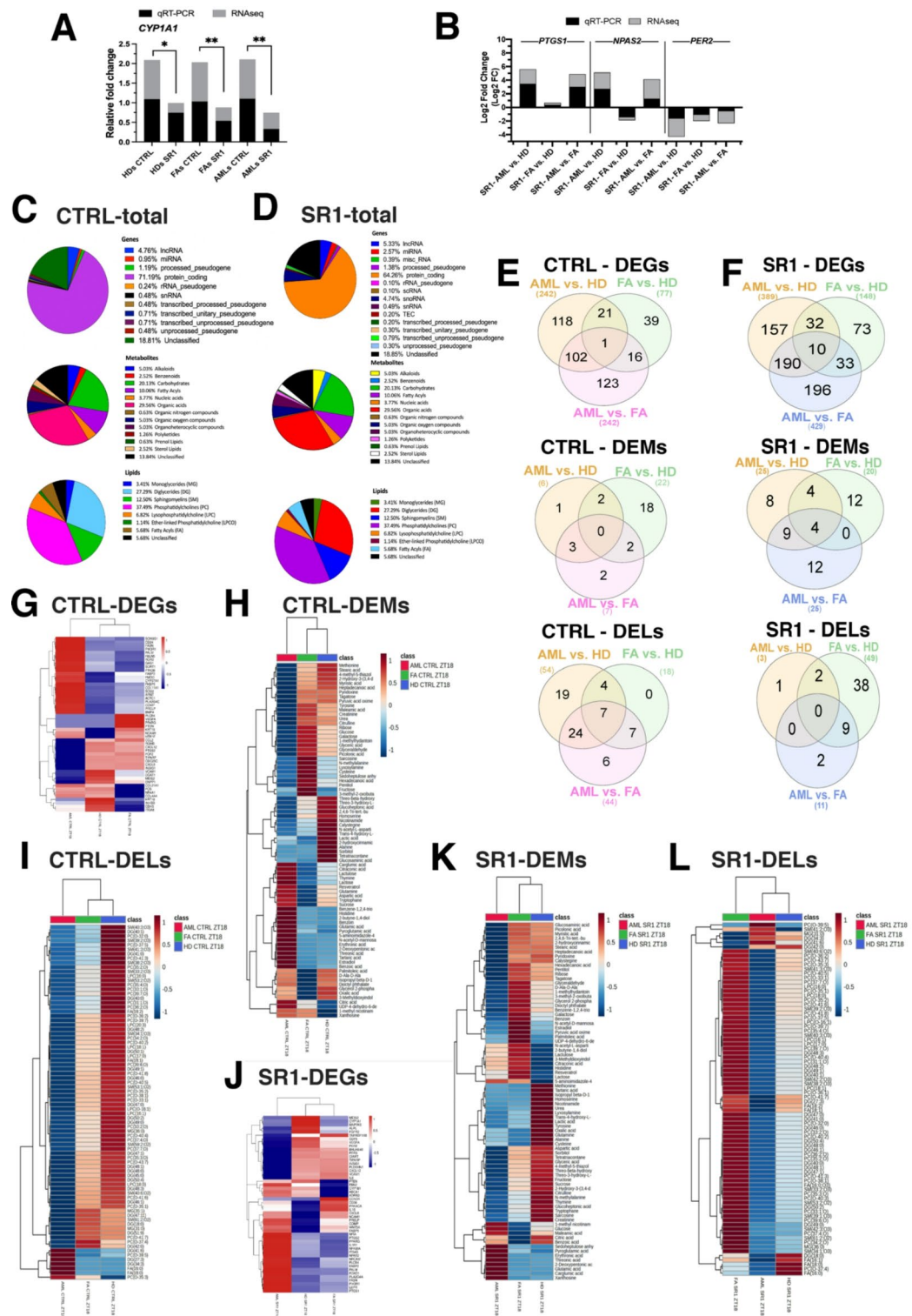
Untreated CTRL (Fig. 4C): In AML vs. HD comparisons (left), pathways such as arginine biosynthesis, fructose and mannose metabolism, and pentose phosphate pathway were significantly enriched ($p < 0.05$). In FA vs. HD comparisons (middle), pathways including galactose metabolism, alanine, aspartate, and glutamate metabolism, and citrate cycle (TCA cycle) were enriched ($p < 0.05$). Lastly, in AML vs. FA comparisons (right), pathways such as pantothenate and CoA biosynthesis, thiamine metabolism, and taurine and hypotaurine metabolism were significantly enriched ($p < 0.05$). Particularly, the arginine biosynthesis pathway stood out in AML comparisons with untreated CTRL groups, whereas its significance was lost after SR1 treatment.

SR1 treatment (Fig. 4D): In AML vs. HD comparisons (left), significantly enriched pathways included arginine biosynthesis, glycerolipid metabolism, pantothenate and CoA biosynthesis, and pentose phosphate pathway ($p < 0.05$). In the FA vs. HD comparison (middle), pathways such as pantothenate and CoA biosynthesis, galactose metabolism, and valine, leucine, and isoleucine biosynthesis were enriched ($p < 0.05$). Lastly, in the AML vs. FA comparison (right), enriched pathways included valine, leucine, and isoleucine biosynthesis, nicotinate and nicotinamide metabolism, and pantothenate and CoA biosynthesis ($p < 0.05$). Notably, the pantothenate and CoA biosynthesis pathway was enriched across all three comparison groups post-SR1 treatment. Detailed information on MSEA is provided in Supplementary Table 10.

Lipid sets enrichment analysis (LSEA) of DELs

LIPEA software was utilized for pathway enrichment analysis of differentially expressed lipids (DELs) identified in three comparative groups, both SR1-treated and untreated. In the AML vs. HD comparison, untreated CTRL groups showed significant enrichment of pathways such as glycerophospholipid metabolism, ether lipid metabolism, and choline metabolism in cancer ($p < 0.05$), while SR1 treatment groups exhibited enrichment in pathways like fatty acid elongation, fatty acid biosynthesis, biosynthesis of unsaturated fatty acids, and fatty acid degradation ($p < 0.05$) (Fig. 5A,B; left). The number of significant lipids in the DELs group decreased from 54 in the untreated CTRL group to 3 after SR1 treatment, with two lipids overlapping between the two groups: DG(51:9) and FA(18:1) (oleic acid) were up-regulated (Supplementary Table 6).

In the FA vs. HD comparison, pathways associated with the sphingolipid signaling pathway, necroptosis, and choline metabolism in cancer were enriched in both untreated CTRL and SR1 treatment groups ($p < 0.05$) (Fig. 5A,B; middle). Although the same pathways were enriched, the lipid contents within each comparison



mostly differed. However, overlapping lipids (diglycerides (DG) and phosphatidylcholine (PC) class) increased by approximately 1-fold following SR1 treatment (Supplementary Table 7).

Similar patterns were observed in the AML vs. FA comparison, with pathways related to glycerophospholipid metabolism, necroptosis, and choline metabolism in cancer enriched in untreated CTRL groups, while pathways associated with glycerophospholipid metabolism, ether lipid metabolism, and choline metabolism in cancer were enriched in groups treated with SR1 ($p < 0.05$) (Fig. 5A,B; right). In both SR1 treatment and untreated controls, 26 common DELs were downregulated, but their expression was less negative after SR1 treatment. The average fold increase of these overlapping 26 lipids after treatment compared to control was 0.861 (Supplementary Table 8).

◀ **Fig. 2.** Comprehensive profiling of genes, metabolites, and lipids of CTRL and SR1 groups. (A,B) Stacked bar graphs represent transcript levels determined by two methods: black bars indicate relative transcript levels measured using qRT-PCR, while gray bars represent transcript levels obtained via RNA-seq. The results are presented as averages of three technical replicates from three biological samples for qRT-PCR and paired-end reads from three biological replicates for RNA-seq. (A) AhR target gene *CYP1A1*, normalized to the CTRL group, was confirmed using qRT-PCR. This confirmed the differential expression observed in the RNA-seq analysis. Significance is indicated by * for $p \leq 0.0332$ and ** for $p \leq 0.0021$. (B) Additionally, three genes (*PTGS1*, *NPAS2*, *PER2*) selected from RNA-seq results were validated in comparison groups under SR1 treatment, ensuring the reliability of the RNA-seq data. These genes were not differentiated (n.d.) in the untreated control (CTRL) groups based on RNA-seq data. (C,D) Multi-omics analysis of BMAT-MSCs revealed distinct classes of total genes (up), metabolites (middle), and lipids (down) using pie charts, showing the distribution of these molecules in the untreated CTRL groups and the SR1 treatment groups, respectively. (E,F) The visualization depicted the numbers of DEGs (up), DEMs (middle), and DELs (down) using Venn diagrams, with overlapping areas representing common genes, metabolites, and lipids between the untreated CTRL groups and the SR1 treatment groups. (G,I) Heatmaps illustrated the expression patterns of 50 DEGs, (H,K) 80 DEMs, and (J,L) 80 DELs, providing insights into differential expression in the untreated CTRL groups and the SR1 treatment groups, respectively, highlighting key differences in molecular profiles. The graphs were generated using GraphPad Prism v9.0.1 (A–D), InteractiVenn webtool (<https://interactivenn.net/>) (E,F), GraphBio webtool (<http://www.graphbio1.com/en/>) (G,I), and MetaboAnalyst v6.0 webtool (<https://www.metaboanalyst.ca/>) (H,I,K,L).

Multi-omics integration of circadian regulation-based transcriptomics and metabolomics through AHR Inhibition

In summary, the detailed elucidation below clearly demonstrates the success of the integration analysis in identifying distinct pathway networks and their associated DEGs, DEMs, and DELs involved in the circadian regulation of AHR inhibition. This underscores the efficacy of the integrated approach in elucidating complex molecular interactions underlying intricate biological processes. Further detailed explanations follow below.

Lipid pathway analysis

The network of lipid subclasses and fatty acid (FA) pathways in untreated CTRL and treated SR1 groups among the three comparative groups is presented in Fig. 5C,D, respectively.

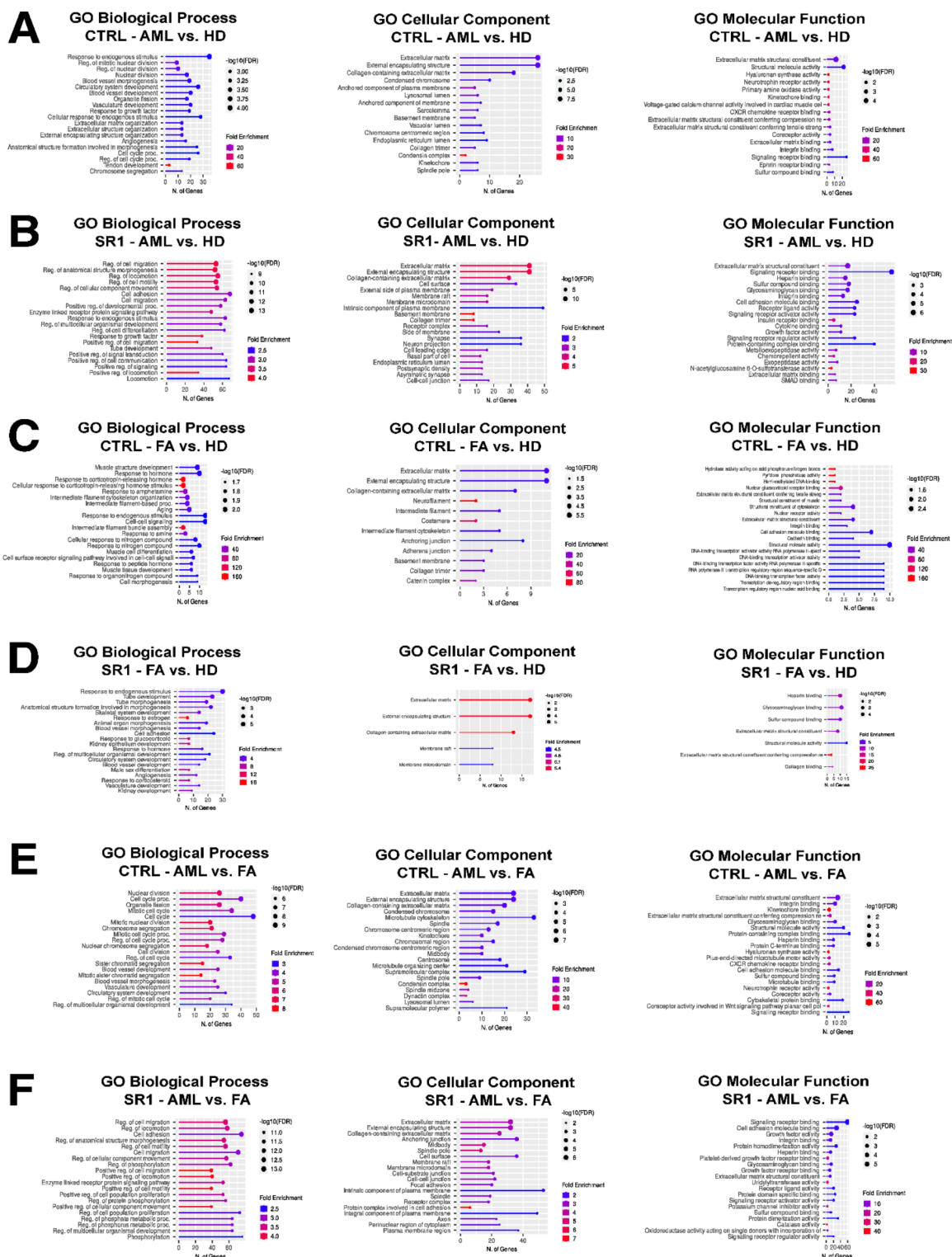
In the untreated CTRL group, fatty acids exhibited the most suppressed pathways among the three comparative groups. In the treated SR1 groups, no reactions or pathways were found after SR1 treatment in contrast to the AML vs. HD comparisons. However, the FA vs. HD comparisons revealed that the most active pathway for fatty acids was FA(16:1) (palmitoleic acid) → FA(18:1) (oleic acid), whereas the most suppressed pathway was FA(16:0) (palmitate/palmitic acid) → FA(18:0) (stearic acid), with respective Z-scores of 1.901 and 2.252. In the latest comparisons between AML and FA, the active pathway for lipid species was DG(47:0) → MG(31:0) with Z-scores of 1.966, while the suppressed pathway for lipid species included MG(31:0) → DG(47:1), MG(31:0) → DG(49:1), MG(31:0) → DG(47:0), and MG(31:0) → DG(49:0) related to triglycerol biosynthesis (triglycerol metabolism), with respective Z-scores of 1.831, 1.794, 1.761, and 1.708. Additionally, there was a significant increase in MG(31:0) synthesis and a simultaneous decrease in DG(47:0). The active pathway for fatty acids was found to be FA(16:0) (palmitate/palmitic acid) → FA(16:1) (palmitoleic acid), FA(16:0) (palmitate/palmitic acid) → FA(18:0) (stearic acid), while the most suppressed pathway was FA(16:1) (palmitoleic acid) → FA(18:1) (oleic acid) → FA(18:2) (linoleic acid), with respective Z-scores of 2.305 and 2.012.

Joint pathway analysis

As a result of the Joint-pathway analysis, we generated six tables for three comparative groups (Supplementary Table 11, all pathways of AML vs. HD, FA vs. HD, AML vs. FA; SR1 and CTRL, respectively), each comprising circadian-controlled pathways of DEGs and DEMs in SR1 treatment (Tables 1, 2 and 3, respectively) and overlapped significant pathways between SR1 treatment and untreated CTRL (Supplementary Tables 12–14). A total of 51 altered pathways were identified in the AML vs. HD groups with SR1 treatment ($p < 0.05$) (Table 1), focusing on 10 circadian-controlled pathways (Table 1). Notable pathways with impact values exceeding 0.1 included regulation of lipolysis in adipocytes (0.1), insulin signaling pathway (0.42), and circadian rhythm (0.5) (Fig. 6A). Additionally, 17 altered pathways were observed in the untreated CTRL, with 7 pathways showing overlapping significant changes between SR1 treatment and untreated CTRL, notably NF-kappa B signaling pathway (0.09, 0.05) and estrogen signaling pathway (0.25, 0.05) (Fig. 6B, Supplementary Table 12).

In the FA vs. HD comparison, 28 altered pathways were identified with SR1 treatment, focusing on 8 circadian-controlled pathways (Table 2). Notable pathways included cellular senescence (0.18) and endocrine resistance (0.2) (Fig. 6C). Like AML vs. HD, slight increases in impact values were observed for most pathways after SR1 treatment. In the untreated CTRL group of the FA vs. HD comparison, 16 altered pathways were identified ($p < 0.05$). Furthermore, we identified 4 pathways exhibiting overlapping significant changes between SR1 treatment and untreated CTRL. The impact values for SR1 and CTRL are provided in parentheses for these pathways. They encompass the Estrogen signaling pathway (0.09, 0.04), ECM-receptor interaction (0.1, 0.19), Prion diseases (0.03, 0.05), and Mineral absorption (0.02, 0) (Fig. 6D, Supplementary Table 13).

For the AML vs. FA comparison, 17 altered pathways were identified with SR1 treatment, focusing on 10 circadian-controlled pathways (Table 3). Notable pathways included the HIF-1 signaling pathway and fatty acid biosynthesis, with high impact values (Fig. 6E). Additionally, one pathway displaying overlapping significant



changes between SR1 treatment and untreated CTRL was detected, including Pathways in Cancer (Fig. 6F, Supplementary Table 14). An increase in impact values was observed for this pathway after SR1 treatment.

STITCH interactions

To group genes and metabolites based on their interactions from STITCH, we used Markov clustering (MCL) via Cytoscape v3.10.1. We set the granularity parameter (inflation value) to 1, 2, or 4, and the confidence score cutoff to 0.4 as their defaults.

In the untreated CTRL group for AML vs. HD comparisons (Fig. 7A), the STITCH interaction network highlighted eight clusters of DEGs and DEMs. By merging the smallest clusters into larger ones based on joint pathway analysis, we reduced the clusters to four. These clusters were identified by associated pathways. The total network visualized 42 nodes and 80 edges (granularity parameter set to 2). *CTSD*, *ACTC1*, and *SEAP2* genes

◀ **Fig. 3.** Gene ontology term enrichment analysis of CTRL and SR1 groups. (A–F) are structured as follows: Gene Ontology-Biological Process (GO-BP) is shown in the first column (left), Gene Ontology-Cellular Component (GO-CC) in the second column (middle), and Gene Ontology-Molecular Function (GO-MF) in the third column (right). Horizontally, the figures compare AML versus HD in the first and second rows, FA versus HD in the third and fourth rows, and AML versus FA in the fifth and sixth rows. Panels (A), (C), and (E) depict comparisons under CTRL conditions, while panels (B), (D), and (F) show comparisons under SR1 treatment. (A–F), lollipop plots illustrate pathways sorted by gene count on the x-axis, with point sizes representing $-\log_{10}(\text{FDR})$ values and colors indicating fold enrichment. The x-axis represents the number of genes per pathway, with a color gradient ranging from red (high fold enrichment) to blue (low fold enrichment). Larger dots indicate pathways with lower $-\log_{10}(\text{FDR})$ values, highlighting their statistical significance. This visualization assists in identifying significantly enriched GO terms, with the color gradient providing a clear distinction between high and low fold enrichment levels. For example, pathways with larger dots and red hues are highly significant, while those with blue and smaller dots show lower significance. All graphs were generated using ShinyGO v8.0 (<http://bioinformatics.sdstate.edu/go/>) webtool.

were singletons and not shown. After SR1 treatment, interactions revealed five clusters of DEGs and DEMs with a granularity parameter of 4. The two smallest clusters were merged, resulting in four consolidated clusters, consisting of 42 nodes connected by 80 edges. Singleton genes *SORBI* and *FASN* were removed (Fig. 7B).

For FA vs. HD comparisons' untreated CTRL group (Fig. 7C), one cluster encompassing related pathways was detected. A network of 18 nodes connected by 30 edges was generated with a granularity parameter of 1. The singleton tryptophan metabolite was removed. With SR1 treatment, two distinct clusters were revealed. This resulted in an interaction network of 13 nodes connected by 16 edges, with the granularity parameter set to 4. No singletons were detected (Fig. 7D).

In the AML vs. FA comparison's untreated CTRL analysis (Fig. 7E), one cluster like FA vs. HD comparison was found, comprising related pathways. A STITCH interaction network of 30 nodes connected by 168 edges was conducted, with a granularity parameter of 4. The singleton gene *GSTT2B* was removed. After SR1 treatment, the number of clusters was reduced from seven to four by merging the smallest clusters into larger ones based on joint pathway analysis. This resulted in an interaction network of 35 nodes connected by 60 edges, with the granularity parameter adjusted to 4. Singleton genes *TBC1D4*, *SLC22A3*, *PLCB4*, and *WASF3* were removed due to no connections (Fig. 7F).

Discussion

To our knowledge, this study is the first in the literature to dissect the crosstalk between the AHR signaling pathway and circadian rhythm in the context of AML, with a focus on BMAT-MSCs. It has been well demonstrated in the literature that hematological malignancies are associated with significant alterations in the BM microenvironment usually initiated by the intrinsic events in the preleukemic cells^{33,34}. There is limited data on the driver role of the BM microenvironment, leading to the development of leukemia^{35–39}. Recent studies showed that the bone marrow adipocytes and their progenitors that reside in the BMAT have a dynamic role in shaping the BM niche both under physiological conditions and in leukemia⁴⁰. In this study, to delineate the complex interplay in the leukemic/preleukemic niche through integrated multi-omics analyses, BMAT-MSCs from healthy donors, AML patients, and, as a transitional model, Fanconi anemia (FA) patients were studied. Inherited conditions like FA and environmental exposure to xenobiotics, chronic inflammation, or previous chemotherapy use have all been identified as potential contributors to the development of secondary myeloid malignancies including AML. Our recent study has shown alterations in the BM microenvironment between healthy donors, FA, and AML patients presenting FA as a suitable transitional model to study leukemogenesis⁴¹ and the potential role of BMAT has been addressed⁴².

In the present study to demonstrate the AhR signaling pathway-related alterations associated with AML pathogenesis in BMAT-MSCs a high-affinity AhR antagonist SR1, known to impact the proliferation and differentiation of HSCs, was used⁴³. Studies have shown that by inhibiting AhR, SR1 promotes the self-renewal of HSCs and thus has been utilized for the in vitro expansion of HSCs in clinical transplantation⁴⁴. Furthermore, a recent study demonstrated that SR1-induced AhR inhibition was found to induce the expansion of leukemic CD34+ cells⁴⁵. There is limited research on its impact on BM niche components. On the other hand, the effect of SR1 on circadian rhythm is not well defined, although some studies have suggested an association between SR1 and circadian desynchronization⁴⁶. When comparing the independent enrichment pathways of transcriptomic and metabolomic analyses with the integrated joint-pathway analysis utilizing both genes and metabolites, it becomes evident that the integrated approach yields more comprehensive and reliable results. This is because it considers the interplay between genes and metabolites, providing a holistic understanding of biological processes.

Our findings suggest that SR1 induced AhR signal inhibition, thus circadian rhythm enhancement of BMAT-MSCs altered the molecular event in favor of leukemogenesis. However, starting from the idea that our study may not fully mimic the findings observed in in vivo animal models, circadian synchronization was conducted to enhance the accuracy and reliability of the in vitro experimental methods. External synchronization signals, such as dexamethasone exposure are used to align cellular clocks in the absence of light, which serves as a natural time cue⁴⁷. In vitro, cultured cells could regain proper circadian rhythm through this entrainment method. Entrainment aids in comprehending the role of cellular regulators and mimicking the in vivo environment, as the cellular response to environmental factors like drugs and xenobiotics varies depending on the circadian phase⁴⁹.

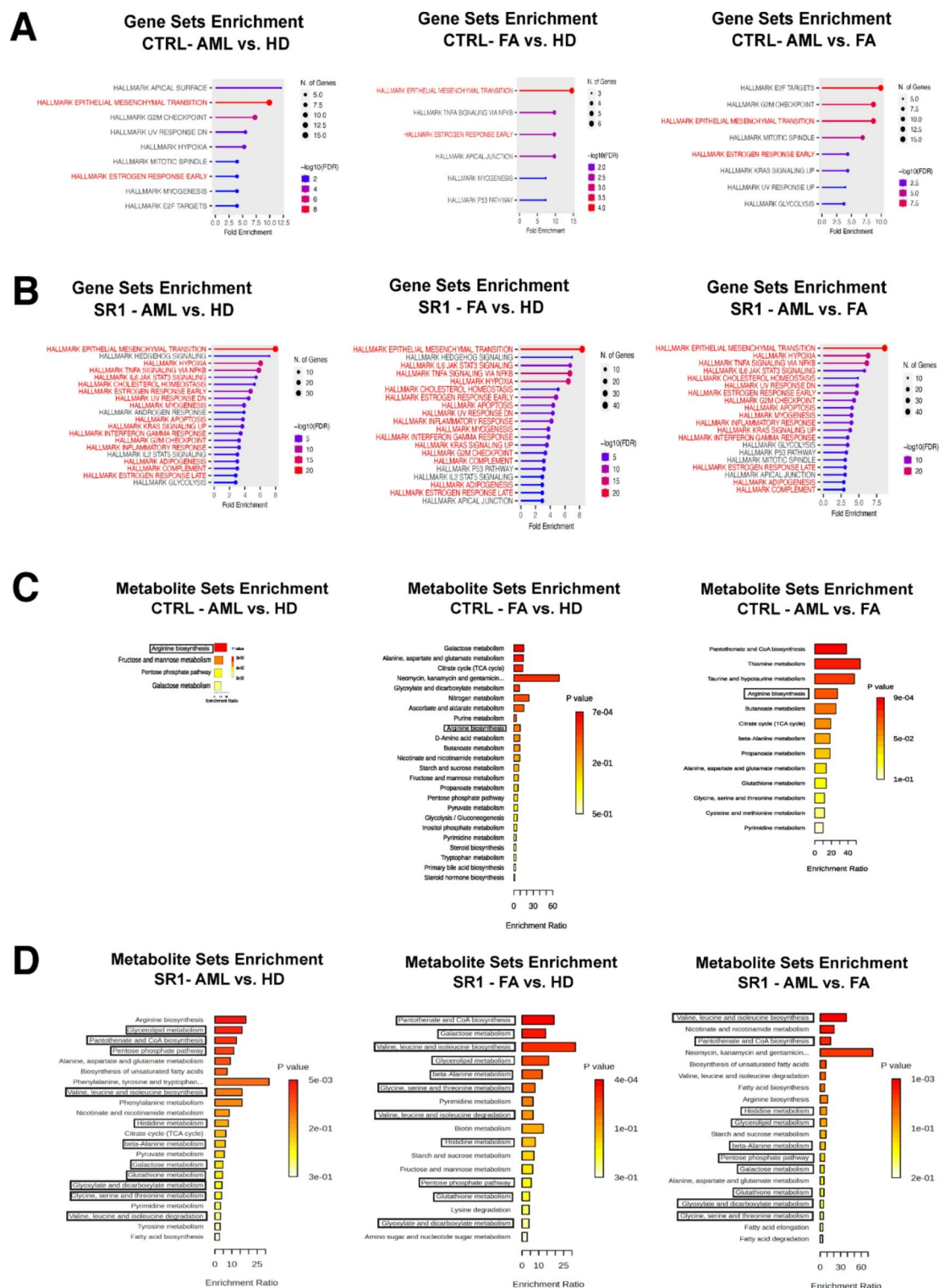


Fig. 4. Gene and metabolite sets enrichment analysis of CTRL and SR1 groups. (A–D) Representing comparisons of AML vs. HD (left), FA vs. HD (middle), and AML vs. FA (right) in the untreated CTRL and SR1 treatment groups. (A,B) Gene Set Enrichment Analysis (GSEA) highlighted significantly overlapped pathways in all three comparison groups, with key hallmarks marked in red for the untreated CTRL (A) and SR1 treatment (B) groups. Gene sets were identified using the MSigDB hallmark collection with an FDR threshold of 0.05. (C,D) Metabolite Set Enrichment Analysis (MSEA) illustrated pathways with significant overlaps within the outlined rectangles for the untreated CTRL (C) and SR1 treatment (D) groups, with a significance threshold of $p < 0.05$. Panels (A,B) were generated using ShinyGO v8.0 (<http://bioinformatics.sdstate.edu/go/>) webtool, and panels (C,D) were generated using MetaboAnalyst v6.0 webtool.

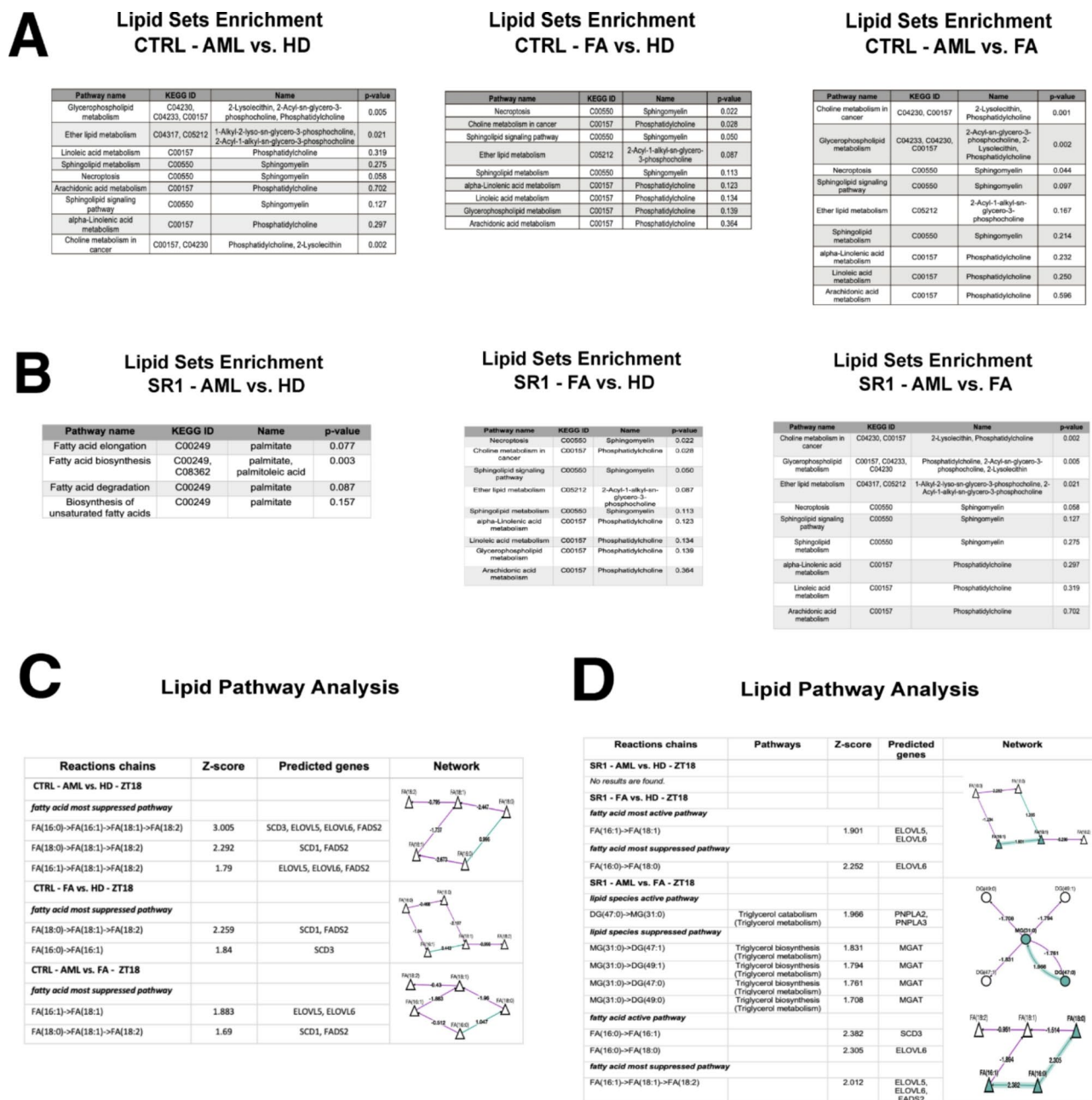


Fig. 5. Lipid sets enrichment and pathway analysis of CTRL and SR1 groups. (A,B) Representing comparisons of AML vs. HD (left), FA vs. HD (middle), and AML vs. FA (right) in the untreated CTRL and SR1 treatment groups. Lipid enrichment analysis (LSEA) exhibited distinct metabolic signatures and underscored potential therapeutic effects on lipid metabolism in (A) the untreated CTRL and (B) SR1 treatment groups using LIPEA software (<https://lipea.biotech.tu-dresden.de>). This analysis highlighted specific lipid pathways and their variations across the treatment conditions. (C,D) The lipid pathway analysis using BioPAN (<https://www.lipidmaps.org/biopan>) software depicted the network of lipid species and fatty acid pathways, providing a comprehensive overview of lipid metabolism changes in response to SR1 treatments. Lipid species and fatty acid pathways are illustrated, showing their interactions and the most active and/or suppressed pathways under (C) the untreated CTRL and (D) SR1 treatment groups.

AhR is a well-defined xenobiotic interacting pathway and the suppression of AhR activity significantly diminishes migration, invasion, and proliferation of cancer cells^{49,50}. Moreover, there are effects of also circadian rhythm on many associated phenotypes. Korkmaz et al. reported an up-regulation consistent with the observed phenotype, as deletion of BMAL1 resulted in increased cell motility and invasion capacity⁵¹. Our study demonstrated significant hallmarks, particularly hallmark EMT and apoptosis, within the comparative groups treated with SR1 (Fig. 4B). Notably, these enriched hallmarks also overlapped with the untreated CTRL groups (Fig. 4A). Following SR1 treatment, there was at least a two-fold increase in enriched genes compared to

Pathway	KEGG ID	Name	CTRL (Log2 FC)	SR1 (Log2 FC)
Regulation of lipolysis in adipocytes	hsa:10,000	<i>AKT3</i>	n.d.	– 2.89
	hsa:5742	<i>PTGS1</i>	n.d.	2.15
	hsa:5295	<i>PIK3R1</i>	n.d.	2
	hsa:8660	<i>IRS2</i>	n.d.	3.53
	C00116	glycerol	n.d.	– 0.54
Insulin signaling pathway	hsa:2194	<i>FASN</i>	1.63	2.92
	hsa:10,580	<i>SORBS1</i>	2.79	3.19
	hsa:10,000	<i>AKT3</i>	n.d.	– 2.89
	hsa:2308	<i>FOXO1</i>	n.d.	3.34
	hsa:3099	<i>HK2</i>	n.d.	– 1.24
	hsa:5295	<i>PIK3R1</i>	n.d.	2
Cellular senescence	hsa:8660	<i>IRS2</i>	n.d.	3.53
	hsa:5608	<i>MAP2K6</i>	n.d.	– 3.63
	hsa:10,000	<i>AKT3</i>	n.d.	– 2.89
	hsa:2308	<i>FOXO1</i>	n.d.	3.34
	hsa:3486	<i>IGFBP3</i>	n.d.	– 2.12
	hsa:5295	<i>PIK3R1</i>	n.d.	2
Circadian rhythm	hsa:4616	<i>GADD45B</i>	n.d.	1.05
	hsa:8863	<i>PER3</i>	n.d.	– 2.2
	hsa:8553	<i>BHLHE40</i>	n.d.	– 1.27
	hsa:4862	<i>NPAS2</i>	n.d.	2.42
Adipocytokine signaling pathway	hsa:8864	<i>PER2</i>	n.d.	– 2.68
	hsa:3953	<i>LEPR</i>	n.d.	2.15
	hsa:10,000	<i>AKT3</i>	n.d.	– 2.89
	hsa:948	<i>CD36</i>	n.d.	2.19
Phospholipase D signaling pathway	hsa:8660	<i>IRS2</i>	n.d.	3.53
	hsa:5332	<i>PLCB4</i>	n.d.	2.03
	hsa:10,000	<i>AKT3</i>	n.d.	– 2.89
	hsa:2185	<i>PTK2B</i>	n.d.	3.25
	hsa:5321	<i>PLA2G4A</i>	n.d.	1.91
	hsa:5295	<i>PIK3R1</i>	n.d.	2
Insulin resistance	hsa:4254	<i>KITLG</i>	n.d.	– 1.09
	hsa:10,000	<i>AKT3</i>	n.d.	– 2.89
	hsa:2308	<i>FOXO1</i>	n.d.	3.34
	hsa:948	<i>CD36</i>	n.d.	2.19
	hsa:5295	<i>PIK3R1</i>	n.d.	2
Type II diabetes mellitus	hsa:8660	<i>IRS2</i>	n.d.	3.53
	hsa:3099	<i>HK2</i>	n.d.	– 1.24
	hsa:5295	<i>PIK3R1</i>	n.d.	2
Sphingolipid signaling pathway	hsa:8660	<i>IRS2</i>	n.d.	3.53
	hsa:5332	<i>PLCB4</i>	n.d.	2.03
	hsa:10,000	<i>AKT3</i>	n.d.	– 2.89
	hsa:1509	<i>CTSD</i>	2.01	2.02
	hsa:427	<i>ASAH1</i>	n.d.	1.07
Circadian entrainment	hsa:5295	<i>PIK3R1</i>	n.d.	2.00
	hsa:8863	<i>PER3</i>	n.d.	– 2.20
	hsa:2353	<i>FOS</i>	n.d.	5.09
	hsa:5332	<i>PLCB4</i>	n.d.	2.03
	hsa:8863	<i>PER2</i>	n.d.	– 2.68

Table 1. AML vs. HD-circadian-controlled pathways of DEGs and DEMs from joint pathways analysis in SR1 treatment.

untreated CTRL, particularly in the context of EMT genes, which correlated with the enhanced motility, adhesion invasion and migration phenotype (Fig. 3B; middle). In all comparative groups, AhR inhibition through SR1 treatment in BMAT cells induced EMT, particularly in AML patients. It is well-defined in cancer cells that EMT is associated with an aggressive phenotype together with increased invasive and metastatic properties⁵².

Pathway	KEGG ID	Name	CTRL (Log2 FC)	SR1 (Log2 FC)
Cellular senescence	hsa:5608	MAP2K6	n.d.	- 3.49
	hsa:595	CCND1	n.d.	1.24
	hsa:10,111	RAD50	n.d.	- 2.72
	hsa:5728	PTEN	n.d.	- 4.87
	hsa:8878	SQSTM1	n.d.	- 4.58
Insulin resistance	hsa:948	CD36	n.d.	3.36
	hsa:5728	PTEN	n.d.	- 4.87
	hsa:9882	TBC1D4	n.d.	1.02
Endocrine resistance	hsa:595	CCND1	n.d.	1.24
	hsa:5566	PRKACA	n.d.	1.95
Pantothenate and CoA biosynthesis	C00106	uracil	n.d.	- 0.63
Focal adhesion	hsa:1311	COMP	n.d.	1.83
	hsa:595	CCND1	n.d.	1.24
	hsa:5728	PTEN	n.d.	- 4.87
ABC transporters	hsa:19	ABCA1	n.d.	- 1.55
	C00135	histidine	n.d.	1.32
	C00116	glycerol	n.d.	- 0.35
Growth hormone synthesis, secretion and action	hsa:5608	MAP2K6	n.d.	- 3.49
	hsa:5566	PRKACA	n.d.	1.95
Fat digestion and absorption	hsa:19	ABCA1	n.d.	- 1.55
	hsa:948	CD36	n.d.	3.36

Table 2. FA vs. HD-circadian-controlled pathways of DEGs and DEMs from joint pathways analysis in SR1 treatment.

However, here we found a similar pattern in the stromal component, the BMAT-MSCs. Previous studies have shown that adipocytes within the tumor microenvironment may transition into their activated form and begin to act like activated adipocytes called cancer-associated fibroblasts⁵³. Our results, which show enrichment in hallmark EMT in AML BMAT-MSCs, particularly after SR1 exposure, are in line with that finding, suggesting education of the microenvironment by leukemic cells. Thus, induction of EMT in AML BMAT-MSCs may suggest their transformation into an activated phenotype towards leukemia/cancer-associated fibroblasts.

Integration of multi-omics data from circadian regulation-based transcriptomics and metabolomics has highlighted overlapping pathways associated with circadian rhythm, circadian entrainment, regulation of lipolysis in adipocytes, and the phospholipase D signaling pathway upon SR1 treatment in AML vs. HD and AML vs. FA, excluding FA vs. HD comparisons. It is worth that the circadian rhythm pathway revealed significant downregulation of *CIART* (Supplementary Table 4) and *BHLHE40* transcription factors, as well as significant upregulation of the *NPAS2* gene in both AML vs. HD and AML vs. FA comparisons (Tables 1 and 3). Recent research has shown that palmitate can influence BMAL1 expression and phosphorylation levels, thereby dampening clock gene expression and increasing fatty acid synthesis in adipocytes⁵⁴. However, our data revealed that in AML vs. FA comparisons, palmitic acid, also known as hexadecanoic acid, was significantly downregulated (-1.17 Log2FC) with SR1 treatment. Additionally, *CIART* and *BHLHE40* circadian repressor genes were downregulated. Consistent with our findings, previous studies have demonstrated that palmitate can induce alterations in *CIART* expression. *CIART* and *BHLHE40* repress BMAL1:CLOCK activity via a mechanism dependent on histone deacetylase, serving as transcriptional repressors that impact the core circadian clock machinery^{55,56}. Therefore, it is plausible that circulating lipid metabolites may act as diurnal systemic signals, influencing clock behavior within the BMAT.

Moreover, a study has reported that the expression of *NPAS2* was increased in AML patients and promoted AML cell growth⁵⁷. The present study identified *NPAS2*, *PER2*, *BHLHE40*, *PER3*, and *CIART* as potential biomarkers of circadian rhythm, offering novel markers or targets for the treatment of BMAT-MSCs with hematological malignancies. Further experimental investigation is warranted to comprehensively understand the contribution to AML pathogenesis. On the other hand, our findings indicate that following SR1 treatment, in AML comparison groups, both *PTGS1* and *PIK3R1* genes, which are associated with lipid metabolism, were matched in both regulation of lipolysis in adipocytes and the phospholipase D signaling pathway. However, the specific effects of these genes on lipolysis are not yet fully understood. Nevertheless, due to their association with lipid metabolism, it is conceivable that these genes may play an indirect or direct role in lipolysis processes. The *PTGS1* gene has been validated using qRT-PCR (Fig. 2B). Shafat et al. investigated the interactions between adipocytes and leukemic cells and showed substantial release of free fatty acids through lipolysis in BMAT meeting the energy needs of leukemic cells, thereby facilitating their survival. They also reported that free fatty acids transport by *FABP4* in co-culture⁴. In our study, it is worth mentioning that BMAT-MSCs exhibited differential expression of *FABP5* (a rhythmic gene) and *FABP2* genes, distinct from the FABP population in BMAT adipocytes (*FABP4*). In the comparison between AML and HD, following SR1 treatment, expressions of *FABP5* (n.d.: no differentiated) (n.d., 2.67 Log2FC), *FABP2* (n.d., 3.07 Log2FC), and *CD36* (n.d., 2.19 Log2FC)

Pathway	KEGG ID	Name	CTRL (Log2 FC)	SR1 (Log2 FC)
HIF-1 signaling pathway	hsa:7010	<i>TEK</i>	– 1.90	– 1.94
	hsa:3099	<i>HK2</i>	n.d.	– 1.20
	hsa:3459	<i>IFNGR1</i>	n.d.	1.13
	hsa:3569	<i>IL6</i>	n.d.	– 3.03
	hsa:5295	<i>PIK3R1</i>	n.d.	1.83
	hsa:3162	<i>HMOX1</i>	n.d.	– 1.05
	hsa:284	<i>ANGPT1</i>	n.d.	1.64
Circadian rhythm	hsa:8863	<i>PER3</i>	n.d.	– 2.12
	hsa:8553	<i>BHLHE40</i>	n.d.	– 1.12
	hsa:4862	<i>NPAS2</i>	n.d.	2.86
Choline metabolism in cancer	hsa:2353	<i>FOS</i>	2.20	4.51
	hsa:6581	<i>SLC22A3</i>	n.d.	2.19
	hsa:10,810	<i>WASF3</i>	n.d.	1.19
	hsa:5321	<i>PLA2G4A</i>	n.d.	1.56
	hsa:5295	<i>PIK3R1</i>	n.d.	1.83
	hsa:80,310	<i>PDGFD</i>	n.d.	2.96
Insulin resistance	hsa:9586	<i>CREB5</i>	n.d.	– 2.30
	hsa:5728	<i>PTEN</i>	n.d.	3.61
	hsa:3569	<i>IL6</i>	n.d.	– 3.03
	hsa:4792	<i>NFKBIA</i>	n.d.	1.17
	hsa:5295	<i>PIK3R1</i>	n.d.	1.83
	hsa:9882	<i>TBC1D4</i>	n.d.	– 1.16
Phosphatidylinositol signaling system	hsa:5332	<i>PLCB4</i>	n.d.	1.54
	hsa:3632	<i>INPP5A</i>	n.d.	– 1.15
	hsa:3613	<i>IMPA2</i>	n.d.	2.31
	hsa:5728	<i>PTEN</i>	n.d.	3.61
	hsa:8821	<i>INPP4B</i>	n.d.	– 1.39
	hsa:5295	<i>PIK3R1</i>	n.d.	1.83
Cellular senescence	hsa:595	<i>CCND1</i>	n.d.	– 1.09
	hsa:891	<i>CCNB1</i>	n.d.	– 1.46
	hsa:983	<i>CDK1</i>	– 2.19	– 1.51
	hsa:5728	<i>PTEN</i>	n.d.	3.61
	hsa:8878	<i>SQSTM1</i>	n.d.	4.07
	hsa:3569	<i>IL6</i>	n.d.	– 3.03
	hsa:5295	<i>PIK3R1</i>	n.d.	1.83
Regulation of lipolysis in adipocytes	hsa:155	<i>ADRB3</i>	n.d.	1.33
	hsa:5742	<i>PTGS1</i>	n.d.	1.86
	hsa:5743	<i>PTGS2</i>	n.d.	1.37
	hsa:5295	<i>PIK3R1</i>	n.d.	1.83
Fatty acid biosynthesis	hsa:2194	<i>FASN</i>	1.60	2.40
	C00249	palmitate	n.d.	– 1.17
	C00712	oleic acid	n.d.	– 1.13
Phospholipase D signaling pathway	hsa:5332	<i>PLCB4</i>	n.d.	1.54
	hsa:2185	<i>PTK2B</i>	2.47	2.72
	hsa:5321	<i>PLA2G4A</i>	n.d.	1.56
	hsa:5295	<i>PIK3R1</i>	n.d.	1.83
	hsa:80,310	<i>PDGFD</i>	n.d.	2.96
	hsa:4254	<i>KITLG</i>	n.d.	– 1.10
Circadian entrainment	hsa:8863	<i>PER3</i>	n.d.	– 2.12
	hsa:2353	<i>FOS</i>	n.d.	4.51
	hsa:5332	<i>PLCB4</i>	n.d.	1.54

Table 3. AML vs. FA-circadian-controlled pathways of DEGs and DEMs from joint pathways analysis in SR1 treatment.

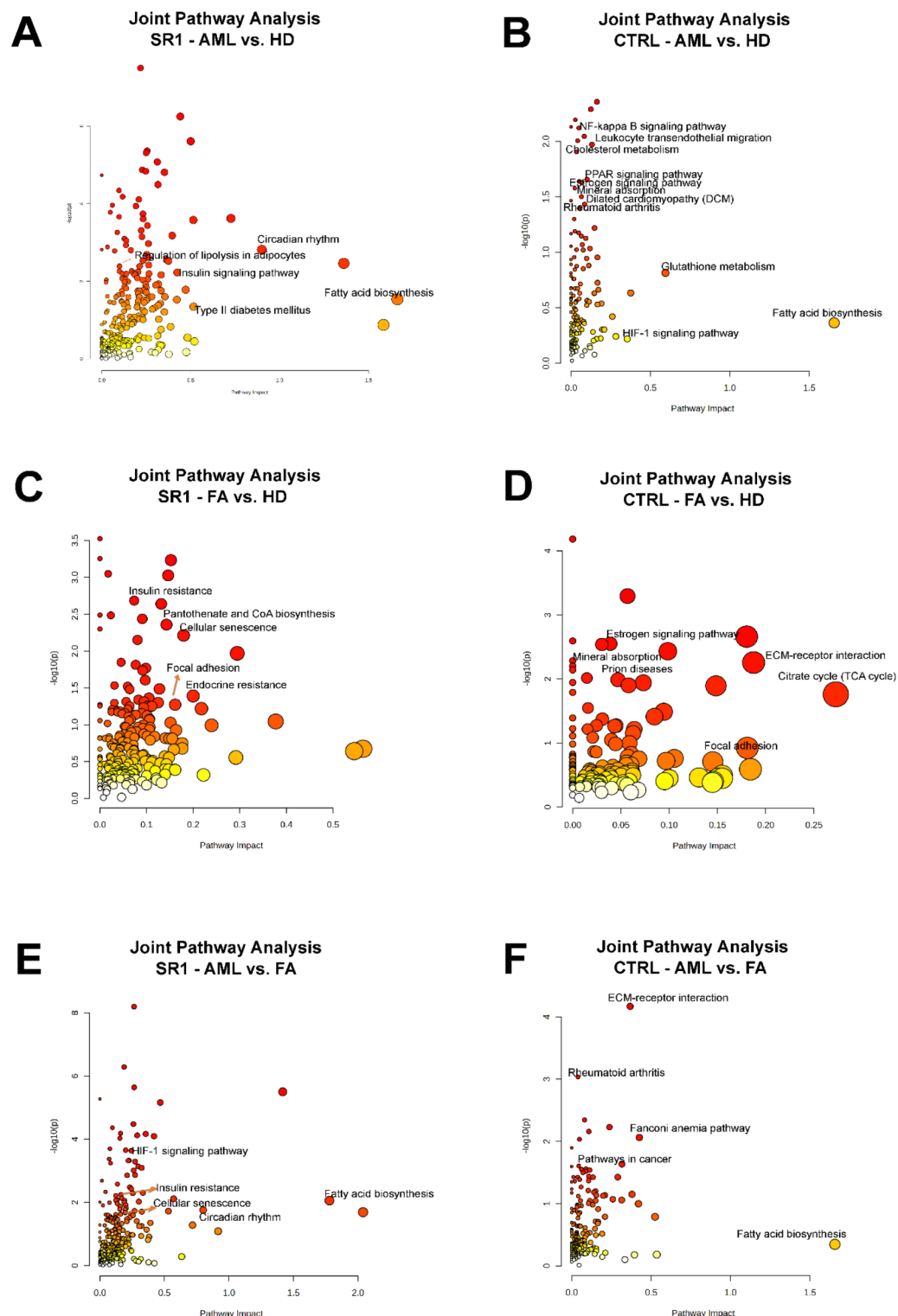
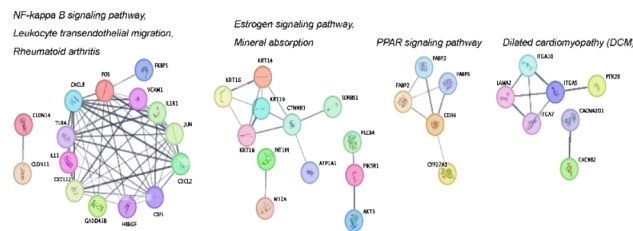
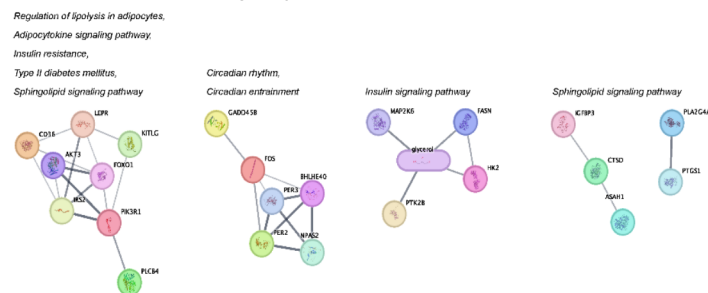
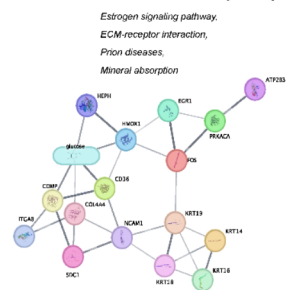
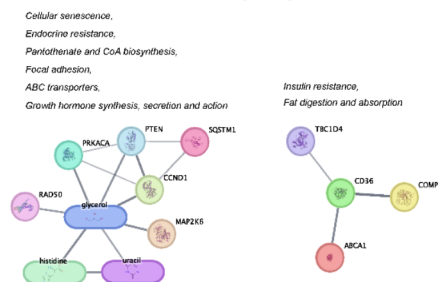
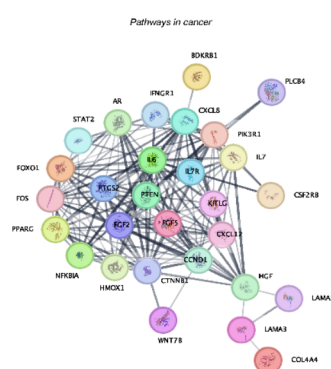
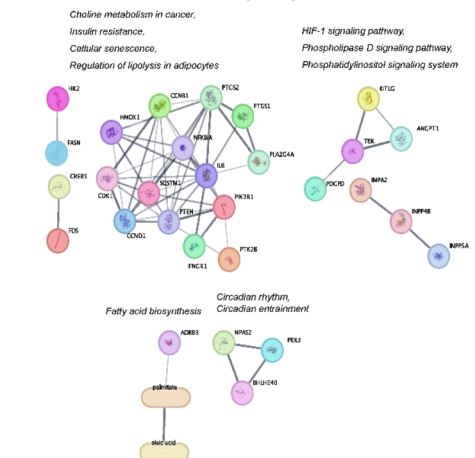


Fig. 6. Joint pathway analysis of SR1 and CTRL groups. (A–F) Joint-pathway analysis using MetaboAnalyst v6.0 webtool was conducted, encompassing all pathways of AML vs. HD (top row), FA vs. HD (middle row), and AML vs. FA (bottom row) to assess significantly altered transcriptomic and metabolomic data in (A,C,E) the SR1 treatment and (B,D,F) the untreated CTRL groups. Each circle in the visualization represents a single metabolic pathway, with the area of the circle proportional to the pathway's impact, and the color gradient indicating pathway significance, ranging from highest (red) to lowest (yellow). The x-axis represents pathway impact, while the y-axis shows $-\log_{10}(\text{p-value})$, indicating the significance of each pathway.

A STITCH Interaction of Joint Pathway Analysis - CTRL - AML vs. HD**B** STITCH Interaction of Joint Pathway Analysis - SR1 - AML vs. HD**C** STITCH Interaction of Joint Pathway Analysis - CTRL - FA vs. HD**D** STITCH Interaction of Joint Pathway Analysis - SR1 - FA vs. HD**E** STITCH Interaction of Joint Pathway Analysis - CTRL - AML vs. FA**F** STITCH Interaction of Joint Pathway Analysis - SR1 - AML vs. FA

were significantly upregulated, while *FABP3* (2.93, n.d. Log2FC) was found to be significantly downregulated, respectively in untreated CTRL and treated SR1 (Supplementary Table 12). Its functions span a diverse spectrum, highlighting the varied roles and associated signaling pathways of *FABP5* in metabolic syndrome, adipogenesis, lipid homeostasis, proliferation, differentiation, metastasis, airway remodeling, inflammation, apoptosis, and autophagic responses⁵⁸. Consistent with our results, involvement of *FABP5* in lipolysis in adipose tissue and fatty acid transport in brain endothelial cells has been reported^{59,60}. The present study may reveal a novel molecular mechanism explaining the upregulation of *FABP5* resulting in increased lipolysis through an AHR-mediated circadian regulation. We also propose that *CD36* might be a key partner for *FABP5* in BMAT-MSC. *CD36* and *FABP5* overexpression and a switch to fatty acid metabolism in tumors have been linked with increased resistance to chemotherapy and correlated strongly with poor prognosis^{61,62}. It is suggested that *FABP5* and *CD36* play a role in cancer development by influencing EMT-related signaling pathways⁶³. In parallel with this

Fig. 7. Schematics of gene-metabolite interactions. (A–F) The STITCH network illustrates interactions between differentially expressed genes (DEGs) and differentially expressed metabolites (DEMs), with adjusted p-values < 0.05 for DEGs (circles) and p-values < 0.05 for DEMs (rounded rectangles). Comparisons are shown for (A) untreated CTRL, (B) SR1 treatment in AML versus HD groups, (C) untreated CTRL, (D) SR1 treatment in FA versus HD groups, and (E) untreated CTRL, (F) SR1 treatment in AML versus FA groups. Markov clustering (MCL) via Cytoscape v3.10.1 was employed to group genes and metabolites based on their interactions from STITCH. The granularity parameter (inflation value) was set to 1, 2, or 4, and the confidence score cutoff was set to 0.4, following default settings. (A–F) The STITCH network illustrates interactions between differentially expressed genes (DEGs) and differentially expressed metabolites (DEMs), with adjusted p-values < 0.05 for DEGs (circles) and p-values < 0.05 for DEMs (rounded rectangles). Comparisons are shown for (A) untreated CTRL, (B) SR1 treatment in AML versus HD groups, (C) untreated CTRL, (D) SR1 treatment in FA versus HD groups, and (E) untreated CTRL, (F) SR1 treatment in AML versus FA groups. Markov clustering (MCL) via Cytoscape v3.10.1 was employed to group genes and metabolites based on their interactions from STITCH. The granularity parameter (inflation value) was set to 1, 2, or 4, and the confidence score cutoff was set to 0.4, following default settings.

context, after SR1 treatment, we demonstrated the enrichment of hallmarks of EMT and the gain of an activated phenotype in BMAT-MSC favoring cancer development. Furthermore, we observed an upregulation of *CD36* and *FABP5* genes in the PPAR signaling pathways. These findings collectively provide potential evidence linking *CD36* and elevated free fatty acids from BMAT-MSCs to AML progression.

Circadian entrainment illustrates how organisms adapt to their environment through Zeitgebers. Our study is the first to demonstrate that exposure to SR1 alters the circadian rhythm in BMAT-MSCs, leading to dysregulation in rhythmicity and homeostasis through AhR-mediated modulation of circadian clocks. These xenobiotic stimuli impact clock gene expression, *PER1* or *PER2*, resulting in decreased expression. In our investigation, we observed a significant decrease in *PER2* expression by -2.68 Log2FC in the AML versus HD group treated with SR1. Furthermore, in both AML versus HD and AML versus FA comparison groups under SR1 treatment, we demonstrated alterations in the expression of *PER3* (-2.20 and -2.12 Log2FC), *FOS* (5.09 and 4.51 Log2FC), and *PLCB4* (2.03 and 1.54 Log2FC) genes, respectively. Recent studies indicate that the absence of *PER3* impacts peripheral oscillators differently through photic signals and is strongly associated with circadian dysfunction in humans^{64,65}. In AML, a study has suggested a potential link between downregulation of circadian clock genes, particularly *PER3*, and dysregulation of the cell cycle, which may promote the proliferation of blastic cells⁶⁶. When considering these genes alongside existing literature, SR1 as a non-photic zeitgeber could potentially regulate photic entrainment responses^{67,68}. Our findings suggest the presence of a photoentrainment phenotype. The intricate molecular mechanisms underlying photic entrainment involve various regulatory factors. Based on our joint pathway analysis, we propose a novel model for the photic entrainment of BMAT-MSCs' circadian clock, particularly in AML stroma, through AhR inhibition. Interestingly, the comparison of the AML group highlights circadian entrainment. In this context, we suggest that the relationship between AhR and the circadian rhythm may be case- or tissue-specific. Overall, our data has provided evidence that xenobiotics may disrupt the physiological balance of the circadian clock system.

In SR1 treatment, lipid pathway analysis findings indicated common but also opposite reactions in comparative groups (FA vs. HD) vs. (AML vs. FA). In the untreated CTRL group, initially, the reactions where stearic acid converts to oleic acid and then to linoleic acid were most suppressed, but these reactions were not observed following SR1 treatment. Research has reported that oleic acid acts as a Zeitgeber on human visceral adipose tissue, subcutaneous adipose tissue, and intestinal and stomach explant cultures via alteration in the circadian rhythm of their clock genes on these tissues. Additionally, they found a significant correlation between oleic acid and circadian core clock genes (*PER2* and *PER3*). Our data supports that both metabolomic and lipidomic analyses show a significant decrease in oleic acid levels in AML vs. HD and AML vs. FA. Additionally, *PER3* gene expression was found to be decreased in both comparisons based on transcriptomic data. However, in the comparisons between FA vs. HD, LIPEA analysis indicates an accumulation of oleic acid in FA. In this comparison, pathways associated with maintaining energy homeostasis were observed such as fat digestion and absorption, ABC transporters, pantothenate, and CoA biosynthesis. It has been reported that 50% of FA patients develop lipid metabolism disorder⁶⁹ and altered lipid metabolism may contribute to BM failure in FA⁷⁰. Moreover, oleic acid-induced lipid accumulation through the regulation of circadian genes has been described⁷¹.

Integrated data reveals overlapping pathways related to cellular senescence and insulin resistance among three comparative groups following SR1 treatment (Tables 1, 2 and 3). Our findings suggest that the upregulation of *PIK3R3* plays a pivotal role in regulating cellular senescence in both AML vs. HD and AML vs. FA comparisons. Furthermore, we observed a significant downregulation of *MAP2K6* in both AML vs. HD and FA vs. HD comparisons. Within both FA vs. HD and AML vs. FA comparisons, the tumor suppressor *PTEN* emerges as a common gene in the cellular senescence pathway, although it is not exclusively associated with this pathway. While no significant difference was observed in the untreated CTRL group for both comparisons (n.d.), *PTEN* exhibited downregulation (-4.87 Log2FC) in the FA vs. HD comparison, but significant upregulation (3.61 Log2FC) in the AML vs. HD comparison. The opposite expression patterns of *PTEN* in these two groups are consistent with the known association of *PTEN*-deficient cells with Fanconi anemia⁷². Interestingly, in our study, *PTEN* emerged as a highly decreased differentially expressed gene following SR1 treatment. *PTEN*-knockout mouse embryonic fibroblasts exhibit cellular senescence because of *PTEN* deficiency⁷³. Moreover, *PTEN* dysfunction is strongly associated with decreased survival rates, chemotherapy resistance, and disease progression in various human cancers⁷⁴.

Mitochondrial dysfunction has been implicated in age-related alterations, thereby contributing to the development of senescent phenotypes⁷⁵. Erythronic acid has represented a novel hallmark in mitochondrial metabolism dysfunction⁷⁶ and in the present study, erythronic acid emerges as the most significantly altered metabolite in both comparison groups following SR1 treatment (AML vs. HD: 3.91 Log2FC, AML vs. FA: 4.41 Log2FC). Finally, in the insulin resistance pathway, there were no significant changes in gene expressions in the three comparison groups under basal conditions (untreated CTRL), whereas DEGs were identified after SR1 treatment. A study examining differences between glucose homeostasis of adipose tissue showed that BMAT adipocytes exhibit resistance to insulin-stimulated glucose uptake compared to brown and white adipose tissue adipocytes⁷⁷. Our findings also indicate that the insulin resistance pathway was affected in all three comparison groups following SR1 treatment in BMAT-MSCs.

Conclusion

In conclusion, the application of integrated RNA transcriptomics, metabolomics, and lipidomic analyses to BMAT of HD, AML, and FA patients indicated the presence of a complex interplay between genes and metabolites in the leukemic/preleukemic niche in both basal state, and particularly after exposure to AhR inhibition by SR1. Furthermore, a close crosstalk between AhR signaling and the circadian rhythm in relevance to myeloid leukemia was demonstrated.

Considering the limited data on the role of BMAT in leukemogenesis in humans, this study, conducted on patients with AML and FA BMAT-MSCs, focuses on AhR signaling and circadian regulation. It has identified potential biomarkers/pathways and lipid metabolite therapeutic candidates that target the circadian rhythm.

Fanconi anemia has emerged as a suitable transitional model to study the development of secondary leukemia. While the findings on AML samples may point to BMAT alterations induced by leukemic cells per se, FA samples reflect primary niche alterations in the preleukemic state, suggesting a possible driver role in developing myeloid neoplasia such as AML. Among the multi-omics presented here, one of the interesting findings is the hallmark EMT, particularly enriched in BMAT-MSCs upon SR1 exposure in both FA and AML patients. This indicates the transformation of adipocytes into an activated phenotype towards cancer-associated fibroblasts even before the development of leukemia in FA.

It is well known that FA patients, due to defective DNA repair are highly susceptible to exposure to mutagenic agents, environmental toxins, and xenobiotics^{23,78}. Given the current results demonstrating significant alterations in BMAT-MSCs between HD, FA, and AML samples, particularly after AhR inhibition it may be suggested that BMAT is a critical tissue serving as a reservoir for dioxins/xenobiotics which may lead to alterations in FA and dysregulated microenvironment in time leading to malignant transformation. The present study brings out candidate pathways and biomarkers that may have implications in hematological diseases including BM failure syndromes and malignancy. There is a need for future studies on human bone marrow samples in relevant diseases to identify therapeutic targets of the marrow microenvironment.

Data availability

The original contributions of this study are detailed in the article and Supplementary Material. Furthermore, the RNA sequencing (RNA-seq) data generated in this study have been deposited in the Gene Expression Omnibus (GEO) database under the accession number GSE283315. For further inquiries, please contact the corresponding authors.

Received: 26 April 2024; Accepted: 5 March 2025

Published online: 12 May 2025

References

- Charbord, P. Bone marrow mesenchymal stem cells: historical overview and concepts. *Hum. Gene Ther.* **21**, 1045 (2010).
- Tirado, H. A., Balasundaram, N., Laaouimiri, L., Erdem, A. A. & Gastel, N. Metabolic crosstalk between stromal and malignant cells in the bone marrow niche. *Bone Rep.* **18**, 2352–1872 (2023).
- Muratoglu, B. et al. Detailed characterization of bone marrow adipose tissue mesenchymal stem cells in healthy donor, Fanconi anemia, and acute myeloid leukemia. *Bone*, 117413. <https://doi.org/10.1016/j.bone.2025.117413> (2025).
- Attané, C. et al. Human bone marrow is comprised of adipocytes with specific lipid metabolism. *Cell. Rep.* **30**, 949–958e6 (2020).
- Shafat, M. S. et al. Leukemic blasts program bone marrow adipocytes to generate a protumoral microenvironment. *Blood* **129**, 1320–1332 (2017).
- Lu, W. et al. Small bone marrow adipocytes predict poor prognosis in acute myeloid leukemia. *Haematologica* **103**, e21–e24 (2018).
- Kumar, B. et al. Acute myeloid leukemia transforms the bone marrow niche into a leukemia-permissive microenvironment through exosome secretion. *Leukemia* **32**, 575–587 (2017).
- Kulkarni, P. S., Crespo, J. G. & Afonso, C. A. M. Dioxins sources and current remediation technologies—A review. *Environ. Int.* **34**, 139–153 (2008).
- Burbach, K. M., Poland, A. & Bradfield, C. A. Cloning of the Ah-receptor cDNA reveals a distinctive ligand-activated transcription factor. *Proc. Natl. Acad. Sci. U S A.* **89**, 8185 (1992).
- Shimba, S. & Watabe, Y. Crosstalk between the AHR signaling pathway and circadian rhythm. *Biochem. Pharmacol.* **77**, 560–565 (2009).
- Gekakis, N. et al. Role of the CLOCK protein in the mammalian circadian mechanism. *Science* **280**, 1564–1569 (1998).
- Gu, Y. Z., Hogenesch, J. B. & Bradfield, C. A. The PAS superfamily: sensors of environmental and developmental signals. *Annu. Rev. Pharmacol. Toxicol.* **40**, 519–561 (2000).
- McIntosh, B. E., Hogenesch, J. B. & Bradfield, C. A. Mammalian Per-Arnt-Sim proteins in environmental adaptation. *Annu. Rev. Physiol.* **72**, 625–645 (2009).
- Lee, Y. Roles of circadian clocks in cancer pathogenesis and treatment. *Exp. Mol. Med.* **53**, 1529–1538 (2021).
- Puram, R. V. et al. Core circadian clock genes regulate leukemia stem cells in AML. *Cell* **165**, 303–316 (2016).
- Bailey, S. M., Udoh, U. S. & Young, M. E. Circadian regulation of metabolism. *J. Endocrinol.* **222**, (2014).

17. Tischkau, S. A. Mechanisms of circadian clock interactions with Aryl hydrocarbon receptor signalling. *Eur. J. Neurosci.* **51**, 379–395 (2020).
18. Jaeger, C. et al. Aryl hydrocarbon receptor deficiency alters circadian and metabolic rhythmicity. *J. Biol. Rhythms.* **32**, 109–120 (2017).
19. Miller, B. H. et al. Circadian and CLOCK-controlled regulation of the mouse transcriptome and cell proliferation. *Proc. Natl. Acad. Sci. U S A.* **104**, 3342 (2007).
20. Zhang, R., Lahens, N. F., Ballance, H. I., Hughes, M. E. & Hogenesch, J. B. A circadian gene expression atlas in mammals: implications for biology and medicine. *Proc. Natl. Acad. Sci. U S A.* **111**, 16219–16224 (2014).
21. Krishnaiah, S. Y. et al. Clock regulation of metabolites reveals coupling between transcription and metabolism. *Cell. Metab.* **25**, 961–974e4 (2017).
22. Garaycoechea, J. I. & Patel, K. J. Why does the bone marrow fail in Fanconi anemia? *Blood* **123**, 26–34 (2014).
23. Pagano, G., Manini, P. & Bagchi, D. Oxidative stress-related mechanisms are associated with xenobiotics exerting excess toxicity to Fanconi anemia cells. *Environ. Health Perspect.* **111**, 1699 (2003).
24. Alter, B. P. Fanconi anemia and the development of leukemia. *Best Pract. Res. Clin. Haematol.* **27**, 214 (2014).
25. Tonyali, G. et al. Simple Isolation of Human Bone Marrow Adipose Tissue-Derived Mesenchymal Stem/Stromal Cells. *Curr. Protoc.* **5**, (2025).
26. Lucas, S. et al. Guidelines for biobanking of bone marrow adipose tissue and related cell types: report of the biobanking working group of the international bone marrow adiposity society. *Front. Endocrinol. (Lausanne).* **12**, 744527 (2021).
27. Eylem, C. C. et al. High-Throughput Single-Step plasma sample extraction optimization strategies with experimental design for LC-MS and GC-MS integrated metabolomics and lipidomics analysis. *Microchem. J.* **179**, 107525 (2022).
28. Bolger, A. M., Lohse, M. & Usadel, B. Trimmomatic: a flexible trimmer for illumina sequence data. *Bioinformatics* **30**, 2114 (2014).
29. Dobin, A. et al. Ultrafast universal RNA-seq aligner. *Bioinf.* **29**, STAR, 15–21 (2013).
30. Trapnell, C. et al. Differential gene and transcript expression analysis of RNA-seq experiments with tophat and cufflinks. *Nat. Protoc.* **7**, 562 (2012).
31. Kanehisa, M. K. E. G. G. Kyoto encyclopedia of genes and genomes. *Nucleic Acids Res.* **28**, 27–30 (2000).
32. Kanehisa, M., Furumichi, M., Sato, Y., Kawashima, M. & Ishiguro-Watanabe, M. KEGG for taxonomy-based analysis of pathways and genomes. *Nucleic Acids Res.* **51**, D587–D592 (2023).
33. Blau, O. et al. Chromosomal aberrations in bone marrow mesenchymal stroma cells from patients with myelodysplastic syndrome and acute myeloblastic leukemia. *Exp. Hematol.* **35**, 221–229 (2007).
34. Li, A. J. & Calvi, L. M. The microenvironment in myelodysplastic syndromes: niche-mediated disease initiation and progression. *Exp. Hematol.* **55**, 3 (2017).
35. Kazianka, L. & Staber, P. B. The bone's role in myeloid neoplasia. *Int. J. Mol. Sci.* **21**, 4712 (2020).
36. Walkley, C. R. et al. A microenvironment-induced myeloproliferative syndrome caused by retinoic acid receptor deficiency. *Cell* **129**, 1097–1110 (2007).
37. Garcia, M. & Chen, C. C. The bone marrow microenvironment-driver of leukemia evolution? *Stem Cell. Investig.* **4**, 11 (2017).
38. McReynolds, L. J. & Savage, S. A. Pediatric leukemia susceptibility disorders: manifestations and management. *Hematol. Am. Soc. Hematol. Educ. Program.* **2017**, 242–250 (2017).
39. Kokkaliaris, K. D. & Scadden, D. T. Cell interactions in the bone marrow microenvironment affecting myeloid malignancies. *Blood Adv.* **4**, 3795–3803 (2020).
40. Pimenta, D. B. et al. The bone marrow microenvironment mechanisms in acute myeloid leukemia. *Front. Cell. Dev. Biol.* **9**, (2021).
41. Özdemir, C. et al. Multiparametric analysis of Etoposide exposed mesenchymal stem cells and Fanconi anemia cells: implications in development of secondary myeloid malignancy. *Clin. Exp. Med.* **23**, 4511–4524 (2023).
42. Uçkan-Çetinkaya, D. & Muratoğlu, B. Response of the bone marrow stem cells and the microenvironment to stress. *Handb. Stem Cell. Ther. Vol.* **1**, 1179–1228. https://doi.org/10.1007/978-981-19-2655-6_22 (2022).
43. Boitano, A. E. et al. Aryl hydrocarbon receptor antagonists promote the expansion of human hematopoietic stem cells. *Science* **329**, 1345–1348 (2010).
44. Walasek, M. A., van Os, R. & de Haan, G. Hematopoietic stem cell expansion: challenges and opportunities. *Ann. N Y Acad. Sci.* **1266**, 138–150 (2012).
45. Gentil, M. et al. Aryl hydrocarbon receptor (AHR) is a novel druggable pathway controlling malignant progenitor proliferation in chronic myeloid leukemia (CML). *PLoS One.* **13**, e0200923 (2018).
46. Guo, J. H. et al. Circadian misalignment on submarines and other non-24-h environments - from research to application. *Mil Med. Res.* **7**, (2020).
47. Balsalobre, A. et al. Resetting of circadian time in peripheral tissues by glucocorticoid signaling. *Science* **289**, 2344–2347 (2000).
48. Ndikung, J. et al. Restoring circadian synchrony in vitro facilitates physiological responses to environmental chemicals. <https://doi.org/10.1016/j.envint.2019.105265> (2019).
49. Elson, D. J. & Kolluri, S. K. Tumor-Suppressive functions of the Aryl hydrocarbon receptor (AhR) and AhR as a therapeutic target in cancer. *Biology (Basel)* **12**, (2023).
50. DiNatale, B. C. et al. Ah receptor antagonism represses head and neck tumor cell aggressive phenotype. *Mol. Cancer Res.* **10**, 1369–1379 (2012).
51. Korkmaz, T. et al. Opposite carcinogenic effects of circadian clock gene BMAL1. *Sci. Rep.* **8**, 16023–16023 (2018).
52. De Craene, B. & Berx, G. Regulatory networks defining EMT during cancer initiation and progression. *Nat. Rev. Cancer.* **13**, 97–110 (2013).
53. Downer, M. A. et al. Understanding the role of adipocytes and fibroblasts in cancer. *Ann. Plast. Surg.* **91**, 779–783 (2023).
54. Tal, Y., Chapnik, N. & Froy, O. Non-obesogenic doses of palmitate disrupt circadian metabolism in adipocytes. *Adipocyte* **8**, (2019).
55. Puig, L. S., Pilon, N. J., Näslund, E., Krook, A. & Zierath, J. R. Influence of obesity, weight loss, and free fatty acids on skeletal muscle clock gene expression. *Am. J. Physiol. Endocrinol. Metab.* **318**, E1–E10 (2020).
56. Gréchez-Cassiau, A. et al. The transcriptional repressor STRA13 regulates a subset of peripheral circadian outputs. *J. Biol. Chem.* **279**, 1141–1150 (2004).
57. Song, B. et al. NPAS2 regulates proliferation of acute myeloid leukemia cells via CDC25A-mediated cell cycle progression and apoptosis. *J. Cell. Biochem.* **120**, 8731–8741 (2019).
58. Xu, B. et al. The biological functions and regulatory mechanisms of fatty acid binding protein 5 in various diseases. *Front. Cell. Dev. Biol.* **10**, (2022).
59. Mitchell, R. W., On, N. H., Bigio, D., Miller, M. R., Hatch, G. M. & D. W. & Fatty acid transport protein expression in human brain and potential role in fatty acid transport across human brain microvessel endothelial cells. *J. Neurochem.* **117**, 735–746 (2011).
60. Hertz, A. V. et al. Lipid metabolism and adipokine levels in fatty acid-binding protein null and Transgenic mice. *Am. J. Physiol. Endocrinol. Metab.* **290**, 814–823 (2006).
61. Pascual, G. et al. Targeting metastasis-initiating cells through the fatty acid receptor CD36. *Nature* **541**, 41–45 (2017).
62. Wang, W. et al. FABP5 correlates with poor prognosis and promotes tumor cell growth and metastasis in cervical cancer. *Tumor Biol.* **37**, 14873–14883 (2016).
63. Nath, A., Li, I., Roberts, L. R. & Chan, C. Elevated free fatty acid uptake via CD36 promotes epithelial–mesenchymal transition in hepatocellular carcinoma OPEN. *Nat. Publ. Group.* <https://doi.org/10.1038/srep14752> (2015).
64. Pereira, D. S. et al. The effect of different photoperiods in circadian rhythms of per3 knockout mice. *Biomed. Res. Int.* (2014).

65. Pendergast, J. S., Niswender, K. D. & Yamazaki, S. Tissue-Specific function of Period3 in circadian rhythmicity. *PLoS One*. **7**, 30254 (2012).
66. YANG, M. Y. et al. Up-regulation of PER3 expression is correlated with better clinical outcome in acute leukemia. *Anticancer Res.* **35**, (2015).
67. Ashton, A., Foster, R. G. & Jagannath, A. Photoc entrainment of the circadian system. *Int. J. Mol. Sci.* **23**. <https://doi.org/10.3390/ijms23020729> (2022).
68. Park, D. et al. Translation of clock rhythmicity into neural firing in suprachiasmatic nucleus requires mGluR-PLC β 4 signaling. *Nat. Neurosci.* **6**, 337–338 (2003).
69. Giri, N., Batista, D. L., Alter, B. P. & Stratakis, C. A. *Endocr. Abnormalities Patients Fanconi Anemia* <https://doi.org/10.1210/jc.2007-0135> (2007).
70. Ravera, S. et al. Altered lipid metabolism could drive the bone marrow failure in Fanconi anaemia. *Br. J. Haematol.* **184**, 693–696 (2019).
71. Li, R. et al. Capsaicin attenuates oleic Acid-Induced lipid accumulation via the regulation of circadian clock genes in HepG2 cells. *J. Agric. Food Chem.* **70**, 794–803 (2022).
72. Vuono, E. A. et al. The PTEN phosphatase functions cooperatively with the Fanconi anemia proteins in DNA crosslink repair. *Sci. Rep.* **6**, (2016).
73. Jung, S. H. et al. mTOR kinase leads to PTEN-loss-induced cellular senescence by phosphorylating p53. *Oncogene* **38**, 1639 (2019).
74. Sharma, A. & Almasan, A. Autophagy and PTEN in DNA damage-induced senescence. *Adv. Cancer Res.* **150**, 249–284 (2021).
75. Yang, T., Wan, R., Tu, W., Avvaru, S. N. & Gao, P. Aryl hydrocarbon receptor: linking environment to aging process in elderly patients with asthma. *Chin. Med. J. (Engl.)*. **137**, 382–393 (2024).
76. Engelke, U. F. H. et al. Mitochondrial involvement and erythronic acid as a novel biomarker in transaldolase deficiency. *Biochim. Biophys. Acta.* **1802**, 1028 (2010).
77. Suchacki, K. J. et al. Bone marrow adipose tissue is a unique adipose subtype with distinct roles in glucose homeostasis. *Nat. Commun.* **11**, (2020).
78. Duxin, J. P. & Walter, J. C. What is the DNA repair defect underlying Fanconi anemia? *Curr. Opin. Cell. Biol.* **37**, 49 (2015).

Acknowledgements

We thank the BMT Unit of Children's Hospital of Hacettepe University, Prof. Barış Kuşkonmaz, and Prof. Fatma Visal Okur for providing bone marrow samples of HD, FA, and AML patients. We thank the Scientific and Technological Research Council of Turkey (TUBITAK) and the Hacettepe University Scientific Research Projects (BAP) Coordination Unit for supporting this study. Additionally, we are grateful for the generous support provided by the Council of Higher Education (CoHE) 100/2000 Ph.D. scholarship program in Turkey.

Author contributions

Conceptualization: D.U.Ç., C.Ö., B.M.; Methodology: B.M., C.Ö., C.C.E., T.R.; Formal analysis and investigation: B.M., C.Ö., İ.Y.; Writing-original draft: B.M., D.U.Ç., C.Ö.; Review and editing: B.M., D.U.Ç., C.Ö., İ.Y., C.C.E., T.R., E.N.; Figures: B.M.; Supervision: D.U.Ç., C.Ö., İ.Y., E.N. All authors contributed to the interpretations of the findings, critically revised the paper, and had final responsibility for the decision to submit for publication.

Funding

This research received funding from the Scientific and Technological Research Council of Turkey (TUBITAK) under grant number 220S759. Partial support was also provided by the Hacettepe University Scientific Research Projects (BAP) Coordination Unit, Project number TDK-2021-19622.

Declarations

Competing interests

The authors declare no competing interests.

Ethics approval

Ethical approval was obtained from the Non-Interventional Clinical Research Ethics Committee of Hacettepe University (Approval Number: GO 21/429 and GO 21/239), and clinical data were collected from patients at Hacettepe Children's Hospital. Informed consent was obtained from their parents or legal guardians. All procedures were conducted following relevant guidelines and standards.

Additional information

Supplementary Information The online version contains supplementary material available at <https://doi.org/10.1038/s41598-025-93169-0>.

Correspondence and requests for materials should be addressed to C.Ö. or D.U.-Ç.

Reprints and permissions information is available at www.nature.com/reprints.

Publisher's note Springer Nature remains neutral with regard to jurisdictional claims in published maps and institutional affiliations.

Open Access This article is licensed under a Creative Commons Attribution-NonCommercial-NoDerivatives 4.0 International License, which permits any non-commercial use, sharing, distribution and reproduction in any medium or format, as long as you give appropriate credit to the original author(s) and the source, provide a link to the Creative Commons licence, and indicate if you modified the licensed material. You do not have permission under this licence to share adapted material derived from this article or parts of it. The images or other third party material in this article are included in the article's Creative Commons licence, unless indicated otherwise in a credit line to the material. If material is not included in the article's Creative Commons licence and your intended use is not permitted by statutory regulation or exceeds the permitted use, you will need to obtain permission directly from the copyright holder. To view a copy of this licence, visit <http://creativecommons.org/licenses/by-nc-nd/4.0/>.

© The Author(s) 2025